Aerothermal Tests of Spherical Dome Protuberances on a Flat Plate at a Mach Number of 6.5

Christopher E. Glass
and L. Roane Hunt

Langley Research Center
Hampton, Virginia

Summary

Aerothermal tests were conducted in the Langley 8-Foot High-Temperature Tunnel at a Mach number of 6.5 on a series of spherical dome protuberances mounted on a flat-plate test apparatus. Detailed surface pressure and heating-rate distributions were obtained for various dome heights and diameters submerged in both laminar and turbulent boundary layers including a baseline geometric condition representing a thermally bowed metallic thermal protection system (TPS) tile. These results form a data base that can be used to predict aerothermal load augmentation for dome protuberances typical of bowed TPS tiles.

The present results indicated that the surface pressures on the domes were increased on the windward surface and reduced on the leeward surface as predicted by linearized small-perturbation theory, and the distributions were only moderately affected by boundary-layer variations. Surface heating rates for turbulent flow increased on the windward surface and decreased on the leeward surface similar to the pressure; but for laminar boundary layers, the heating rates remained high on the leeward surface, probably due to local transition. Transitional flow effects caused heat load augmentation to increase by 30 percent for the maximum dome height in a laminar boundary layer. However, the corresponding augmentation for a dome with a height of 0.1 in. and a diameter of 14 in. representative of a bowed TPS tile was 14 percent or less for either a laminar or turbulent boundary layer.

Introduction

An important design consideration for hypersonic flight vehicles is the thermal protection system (TPS) of the primary structure. Various design candidates of both metallic and ceramic classifications have been fabricated and tested. (See refs. 1 to 4.) Furthermore, the reliability of the ceramic TPS has been established by the successful flight program with the Space Shuttle orbiter. The most recent metallic design, as described in references 5 and 6, features a metallic tile with a low heat-transfer coefficient mechanically attached at each corner to the primary structure. All the various TPS concepts have inherent surface irregularities and/or protuberances that must be addressed both analytically and experimentally for pressure and heat load augmentation. The ceramic TPS concepts were faced with surface gaps between the tiles to allow for thermal and mechanical deflections. (See ref. 1.) The earlier metallic concepts were characterized by a corrugated aerodynamic surface. The corrugations significantly increased local aeroheating when not aligned with the flow, as presented in reference 7. To accommodate the higher thermal loads, higher temperature materials were required with attendant increased mass. The more recent metallic concept has surface irregularities due to bowing of the individual tiles to relieve thermally induced stresses. An array of bowed tiles over the surface of a vehicle would alter the surface profile to a quilted pattern and thus modify the aerothermal pressure and heat loads on the surface.

The flow over wavy surfaces associated with the earlier metallic concepts was studied analytically in references 8 and 9. The most successful methods were empirical (see refs. 7 and 10), but the extrapolation of local flow behavior to large surface areas is the most difficult part of the analysis. The quilted surface pattern of bowed TPS tiles has been analyzed using a full Navier-Stokes solution, and the results are presented in references 11 and 12. The analysis was first applied to a simple spherical dome protuberance with a Mach 7 flow using a flat-plate laminar boundary layer for a sharp leading edge. The dome was modeled with both side boundaries as planes of symmetry representing a single row of domes transverse to the flow. This analysis provides very graphic details of the flow field about domes of various heights from one-half to twice the laminar-boundary-layer thickness. In reference 12 this work is extended to represent the quilted pattern for a series of domes in the flow direction. Again, the complete laminar flow field was obtained and a complex flow was revealed when the domes were diagonally aligned to the flow. This analysis indicated that the heat load of the downstream domes was substantially less than that of the leading dome. The works of references 11 and 12 are major contributions in defining the surface/flow interactions associated with bowed TPS tiles; however, a turbulent-flow model is needed for more realism and experimental results are needed for verification.

The present experimental study was designed to provide data for the verification of the laminar analysis of reference 11 and to provide verification data to extend the study to include larger domes and the turbulent-flow condition. For the present study, the baseline dome simulated a 10- by 10-in. metallic tile that would bow 0.1 in. at the design temperature differential through the tile thickness. The single dome representing this tile was 14 in. in diameter. For the parametric study, the diameter was varied between one-half and twice the baseline diameter. Also, the dome heights were exaggerated by factors of 2 and 4 to establish a trend in the pressure and heating-rate distributions on the domes. Aerothermal tests were made in the Langley 8-Foot High-Temperature Tunnel (8' HTT) at a Mach number

of 6.5, a total temperature of 3300°R, and a unit Reynolds number of 0.3 × 10^6 per foot. Detailed surface pressure and heating-rate distributions were obtained for domes submerged in both laminar and turbulent boundary layers. The results of this study are presented herein and serve as a data base to complement and verify predictions of the augmented aerothermal loads due to the thermally induced bowing of metallic TPS tiles.

Symbols

c_p	specific heat at constant pressure, Btu/lbm-sec
D	dome diameter, in.
H	dome height, in.
M	Mach number
N_{Re}	Reynolds number based on characteristic distance S from leading edge
p	pressure, psia
q	heating rate, Btu/ft²-sec
R	dome radius, in.
r, θ	polar coordinates (fig. 5)
S	distance from panel holder leading edge (fig. 2), in.
T	temperature, °R
t	time
u	velocity in streamwise direction, ft/sec
x, y, z	Cartesian coordinates (fig. 5)
α	angle of attack, deg
γ	ratio of specific heats
Δ	incremental change
δ	velocity boundary-layer thickness, in.
ρ	density, lbm/ft³
τ	skin thickness, in.

Subscripts:

e	boundary-layer edge
fp	flat plate
ip	instrumented plug
max	peak value
R	boundary-layer probe (rake)
t	total
w	wall
1, 2, 3 ...	measurement number
∞	test-chamber free stream

Abbreviations:

B.L.	boundary layer
CD	ceramic dome
L.E.	leading edge
PD	pressure-instrumented dome
TD	thermocouple-instrumented heat-flux dome
2-D	two-dimensional
3-D	three-dimensional

Apparatus and Test

Model

The model consists of various spherical domes mounted on the flat-plate panel holder, shown in figure 1, installed in the Langley 8-Foot High-Temperature Tunnel (8' HTT). Either a laminar or turbulent two-dimensional boundary layer is established over the test surface depending upon the leading-edge configuration. The laminar boundary layer is produced using a 0.38-in-radius blunt leading edge, and the turbulent boundary layer is produced using flow trips with either a blunt or sharp leading edge. The aerodynamic fences, shown in figure 1, are used to maintain two-dimensional flow over the test surface by preventing vorticular flow spillage at angle of attack. The leading edge is solid copper, and the windward surface is covered with 1.0-in-thick ceramic tiles.

The various dome configurations are illustrated in figure 2. Three panel inserts were used to mount the three dome configurations shown at the top of figure 2. As indicated, the smaller domes were configured by mounting the domes side by side to match the analytical modeling of reference 11 and to test various dome combinations. The dome locations shown correspond to the normal positions for the domes. The designations "PD," "TD," and "CD" refer to the pressure-instrumented dome, the thermocouple-instrumented heat-flux dome, and the ceramic dome, respectively. The domes were set into the panel inserts with minimal peripheral gaps of less than 0.030 in. The location of each dome is shown relative to the panel insert and leading edge, and the two leading-edge configurations are indicated. Also, the locations of the instrumented plug and the

boundary-layer probe are indicated. Normally, the surface pressure and the heat flux were measured upstream of the domes using the instrumented plug, and pitot pressure through the boundary layer was measured downstream using the boundary-layer probe. (See fig. 3.)

The nominal dome dimensions are presented in the following table. Dome 4 is the baseline configuration with a diameter of 14 in. and a height of 0.1 in. corresponding to the expected maximum bowed height of a typical metallic tile concept. For the parametric study, the heights were increased to establish surface data trends for the larger protuberance heights. The diameter variation provided a wider range of dome heights relative to boundary-layer thickness for the same H/D ratios. The domes consisted of a 0.50-in-thick disk-shaped base that was recessed below the test surface and an upper spherical portion that protruded above the surface. The domes were fastened to the panel insert with a single stud at their center.

Dome	Diameter, D, in.	Height, H, in.	H/D
1	7	0.05	0.007
2	7	.1	.014
3	7	.2	.028
[a]4	14	.1	.007
5	14	.2	.014
6	14	.4	.028
7	28	.4	.014
8	28	.8	.028

[a]Baseline configuration.

The pressure domes were made of solid stainless steel and the upper spherical portion was machined to match the nominal dimensions. However, the fabrication of heat-flux domes was less precise since thin-wall material was formed and then attached to the base with countersunk screws around the perimeter. The top of the 7- and 14-in-diameter domes was formed with 0.031-in-thick stainless steel, but 0.062-in-thick aluminum was used for the 28-in-diameter dome. Aluminum was used for the larger diameter dome because of fabrication difficulties when using stainless steel; however, only the largest height was successful when using aluminum. A flat 14-in-diameter disk was fabricated for calibration of the surface pressure and the heat flux for each flow condition and is shown schematically in figure 4. The ceramic domes were cast using Resco Cast

RS-17E material (of Resco Products, Inc.) for each height of the two smaller diameters. The ceramic domes were used to provide symmetry about the center dome and to determine the temperature pattern on the surface of an insulating material for comparison with heating patterns obtained from the thin-wall metallic domes. Additional flat ceramic domes were used on each side of the center dome when only one instrumented dome was used.

Instrumentation

The pressure and heat-flux domes were instrumented with 58 sensors distributed as illustrated in figure 5. Sensor locations are presented in table I using polar coordinates r and θ. The pressure domes were instrumented using 0.060-in. inside-diameter stainless-steel tubes mounted through the domes and flush with the outer surface. The tubes were attached to individual electromechanical pressure transducers located inside the panel holder directly below the panel inserts. The heat-flux domes were instrumented with chromel-alumel thermocouples with individual wires spot-welded 0.040 in. apart to the backside of the thin-wall cover sheet. By using the one-dimensional transient heat balance, the local surface heat flux was determined from the slope of the temperature time histories of the thermocouples. Also, the surface temperatures on the ceramic model were measured and recorded by an AGA Thermovision System 680 (AGA-680) infrared scanner mounted directly over the panel.

Additional instrumentation on the panel holder consists of an instrumented plug and a boundary-layer probe as shown schematically in figures 6(a), and 6(b), respectively. The instrumented plug has a Gardon heat-flux gauge and a pressure orifice to measure surface heat flux and static pressure just forward of the dome model. The boundary-layer probe has 14 pitot pressure tubes and 1 static pressure orifice and is used for boundary-layer definition over the panel holder. Typically, the instrumented plug was positioned forward of the dome model and the boundary-layer probe was mounted aft of the dome model. However, for several runs the boundary-layer probe was positioned forward to define the boundary layer just forward of the dome model.

Test Facility

The Langley 8-Foot High-Temperature Tunnel (8' HTT) is a large blowdown tunnel that simulates aerodynamic heating and pressure loading for a nominal Mach number of 7 at altitudes between 80 000 and 120 000 ft. (See fig. 7.) The high energy needed for simulation is obtained by burning a mixture of methane and air under pressure in the combustor

and expanding the products of combustion through a conical-contoured nozzle into the open-jet test chamber. The flow enters a supersonic diffuser where it is pumped by an air ejector through a mixing tube and exhausted to the atmosphere through a subsonic diffuser. The tunnel operates at total temperatures from 2400°R to 3600°R, free-stream dynamic pressures from 250 to 1800 psf, and free-stream unit Reynolds numbers from 0.3×10^6 to 2.2×10^6 per foot, and it has a maximum run time of 120 sec.

The model is stored in the pod below the test stream to protect it from adverse tunnel start-up loads. Once the desired flow conditions are established, the model is inserted into the test stream on a hydraulically actuated elevator. Insertion time is typically 1.5 sec. The model pitch system provides an angle-of-attack range from -20° to 20°. More detailed information about the tunnel can be found in references 13 and 14.

Test Procedure

The flow conditions for the tunnel tests are presented in table II. The tests were made at nominal total temperatures and pressures of 3300°R and 440 psia, respectively, and the free-stream test conditions presented are based on the tunnel surveys and the thermal, transport, and flow properties for the combustion products of methane and air as presented in reference 15. The tests were conducted using three surface flow conditions (cases):

Case 1 - Laminar boundary layer with a blunt leading edge (no trips)

Case 2 - Turbulent boundary layer with a blunt leading edge (with trips)

Case 3 - Turbulent boundary layer with a sharp leading edge (with trips)

Runs 1, 2, 16, 17, 28, and 29 were made with the flat calibration disk in place of the dome model and with the boundary-layer probe in the forward and aft positions for each of the flow conditions. The calibration disk correlated the flat-plate reference conditions at the dome model location to the free-stream total pressure and total temperature. This relationship determined flat-plate pressures and heating rates for the bowed-dome model runs. The boundary-layer probe determined the boundary-layer profile upstream and downstream of the 7- and 14-in-diameter domes. The measured dome heights for various runs are presented in table II.

Typically, the model was in the test stream 5 sec in order to stabilize pressure transducer fluctuations and to obtain time temperature histories from the dome instrumented with thermocouples. However, four model runs were dedicated to AGA-680 infrared

scanner data so that the model was in the test stream 40 sec to let the model surface approach the radiation equilibrium temperature. All tests were made at an angle of attack of 5°.

Data Acquisition and Reduction

Model pressure and temperature and tunnel digital data were recorded on magnetic tape using the on-site 8' HTT computer at a rate of 20 samples per second. The magnetic tapes were then sent to the Langley Central Digital Data Recording Subsystem for processing of the information to useful engineering units on tapes and plots. Model pressure values were selected from the data after steady pressures were established on the surface and in the orifice tubes connecting the transducers. The slope of the temperature time histories of the thermocouples was obtained immediately after the model reached the centerline of the tunnel. Surface heating rates were calculated from these slopes using the one-dimensional transient heat balance equation

$$q = \rho c_p \tau \frac{\Delta T}{\Delta t} \tag{1}$$

The heat flux from the Gardon gauge was reduced directly from the differential thermocouple output that was calibrated in a radiant furnace.

The AGA-680 infrared-scanner analog data are recorded on-site using a 14-track frequency-modulated (FM) tape recorder at a rate of 16 data frames per second. Each frame consists of approximately 100 scan lines with 120 data points per scan line. The FM data tapes are digitized and reduced to temperature-engineering-unit contour plots.

Results and Discussion

Local Flow Field

Undisturbed profiles. Local flow conditions for the three cases of the present tests are characterized by the Mach number profiles presented in table III. The Mach number was calculated from the ratio of static pressure to pitot pressure using inviscid, perfect-gas assumptions. The profile locations were forward and aft of the dome model location at S_R = 58.1 in. and S_R = 89.1 in., respectively. Mach number profiles at the aft location (S_R = 89.1 in.) were measured with the dome model replaced by a flat circular insert so that no disturbance was present forward of the boundary-layer probe. In figure 8 the experimental Mach number data are compared with Mach number profile distributions obtained from a boundary-layer computer program (ref. 16) for case 1 (laminar boundary layer with a blunt leading edge

(no trips)) and case 2 (turbulent boundary layer with a blunt leading edge (with trips)).

In figure 8(a), experimental data from case 1 agree with the laminar boundary layer predicted by the methods of reference 16, thus indicating that a good laminar boundary layer is being produced over the flat-plate panel holder. Note that the experimental data extend beyond the boundary-layer edge into an entropy gradient region that is produced by the curved bow shock associated with a blunt leading edge. The streamline entropy rise is a function of the shock angle through which it passes so that the highest streamline entropy jump will occur through a normal shock (stagnation streamline) and lower entropy jumps will be produced as the shock angle decreases. Thus, as a hypersonic flow field passes through the curved bow shock of a blunt leading edge, an entropy gradient will be produced with higher streamline entropy at the wall and decreasing streamline entropy away from the wall.

Mach number profiles for the turbulent boundary layer with a blunt leading edge (case 2) are shown as figure 8(b). The experimental data for this condition also agree with the "turbulent prediction" of the boundary-layer code (ref. 16) out to the boundary-layer edge showing that a well-developed turbulent boundary layer is being produced by the flow trips for this case. In the turbulent prediction, transition is assumed to begin at the flow trips ($S = 5$ in.) and the flow is fully turbulent at $S = 17$ in. Beyond the edge of the boundary layer, an entropy gradient region explained previously is also present, as seen for case 1 (fig. 8(a)).

Mach number profiles for a turbulent boundary layer with a sharp leading edge (case 3) were obtained using the boundary-layer code (ref. 16), but the resulting boundary-layer thickness did not agree with that determined by the empirical relation

$$\frac{\delta}{S} \approx 0.37 N_{\text{Re}}^{-1/5} \quad (2)$$

taken from reference 17 or with the experimental boundary-layer thickness. The empirical boundary-layer thickness agrees with the experimental boundary-layer thickness for both the forward and aft rake positions as shown in figure 9(a). The experimental Mach number profile was reduced to a velocity profile using the definition of Mach number:

$$\frac{u}{u_e} = \frac{M T^{1/2}}{M_e T_e^{1/2}} \quad (3)$$

Substituting for static temperature using the isentropic relationship from reference 18, equation (3) is

expressed as

$$\frac{u}{u_e} = \frac{M}{M_e} = \frac{\left[T_t \left(1 + \frac{\gamma-1}{2} M_e^2\right)\right]^{1/2}}{\left[T_{t,e} \left(1 + \frac{\gamma-1}{2} M^2\right)\right]^{1/2}} \quad (4)$$

To define the variation in total temperature within the boundary layer, the Crocco relation between total temperature and velocity was used for the present case. This relationship is given in reference 19 as

$$\frac{T_t - T_w}{T_{t,e} - T_w} = \frac{u}{u_e} \quad (5)$$

Therefore, the experimental velocity profile presented in figure 9(b) was computed by iterating with equations (4) and (5). The total temperature was first assumed constant through the boundary layer in equation (4). The resulting velocity profile was used in equation (5) to compute a new total temperature profile that was then used in equation (4) to compute a new velocity profile. This process was repeated until the change in velocity between iterations was negligible. The experimental profile is compared with the classical flat-plate turbulent velocity profile

$$\frac{u}{u_e} = \left(\frac{z}{\delta}\right)^{1/7} \quad (6)$$

as given by reference 20, for both the forward and aft boundary-layer probe locations. The profiles agree exactly for z/δ values greater than about 0.25, but near the wall the experimental velocity is greater than the 1/7th-power-law prediction.

This difference may be due to the initial assumption that Crocco's relation is not satisfied throughout the entire boundary-layer thickness and that difficulties exist in obtaining good, accurate data near the wall. Overall, the comparisons in figure 9 indicate that a good turbulent boundary layer is being produced over the flat-plate panel holder for the sharp leading-edge configuration with flow trips.

Disturbed profiles. Generally, the Mach number profiles of the wake behind the domes for all the flow cases were similar to the undisturbed profiles with a larger variance at the larger dome heights. The profiles for case 1 are presented in figure 10 for the 7, 14, and 28-in-diameter domes with changing dome height. Figure 10 shows that for a constant diameter, increasing dome height increases the Mach number in the boundary-layer-edge region near the wall and decreases the Mach number in the entropy gradient region near the free stream. The increasing Mach number near the wall is believed caused by transition from laminar to transitional flow because of the dome

geometry disturbing the local flow field and causing separation vortices near the dome.

During transition from laminar to turbulent flow, a greater degree of momentum transfer from the free stream to the boundary layer is present. This transfer results in an increase in Mach number starting at the boundary-layer edge and, as the flow becomes turbulent, finally continuing through the boundary layer to the near-wall region. This increase causes the turbulent-boundary-layer profile to be fuller than the laminar-boundary-layer profile. Note that the larger diameter dome shows this effect to a greater extent than the smaller diameter, more shallow domes. The decrease in Mach number with increasing dome heights over the entropy gradient region is believed to be caused by two weak shock systems forward and aft of the dome, as illustrated in the inset in figure 10. As the flow encounters the dome, a small initial region of flow separation occurs because of the adverse pressure gradient behind the initial weak shock system. The flow then expands over the dome through a Prandtl-Meyer expansion region until it encounters the second flow-separation/weak-shock region. The strength of the initial and the second flow-separation/weak-shock regions depends on the dome diameter and height. Most likely, the shifting of the Mach number profiles shown in figure 10 is caused by a combination of these two flow effects, namely, transitional vortices in the boundary layer and weak shocks outside the boundary layer.

The Mach number profiles at the aft boundary-layer probe location for case 2 are presented in figure 11. The effect of dome geometry variation on Mach number in the wake disturbance region behind the dome is similar to that for case 1, i.e., an increasing Mach number in the region near the wall and a decreasing Mach number near the free-stream layer as dome height increases. Again, the inset in figure 10 is helpful in explaining these profile shifts. Mach number increases in the boundary-layer region near the wall are due to the separation vortices causing more momentum transfer from free stream to the boundary layer, and Mach number decreases near the free stream are due to stronger shocks for increasing dome height at a constant dome diameter.

Wake-disturbance Mach number profiles for case 3 are presented in figure 12 for flow over the 14-in-diameter dome with varying height. The profile through most of the boundary layer shows no significant Mach number variation, but the Mach number decreases significantly at the boundary-layer edge as the dome height increases. For case 3 there was no vortical flow effect to increase boundary-layer Mach numbers; however, stronger shocks caused the large decrease in Mach number at the edge of the bound-

ary layer with an increase in dome height. For all dome heights, the Mach number data presented as figure 12 collapse together at $z = 2.5$ in.

Surface Pressure Distributions

Dome pressure measurements, normalized to the flat-plate reference pressure for each run, are presented as table IV for each flow condition. Normalized pressure contours are presented in figure 13 and give an overview of the differences between the three flow cases tested. The effect of dome geometric variation on surface pressure is shown in figure 13 with a dome height increase from left to right and a dome diameter increase from top to bottom. The baseline configuration (the 14-in-diameter dome that is 0.1 in. high ($H/D = 0.007$)) shows little variation in pressure over the dome surface for all three flow cases, thus indicating minimal flow disturbance for actual bowed TPS concepts. However, as the height is increased over the range of H/D variation, the pressure gradients become larger as indicated by the contour density over the dome surface. Note that for the two smaller diameter domes, there is a skewing of pressure contours laterally across the dome surface. Referring to figure 2 for the 7- and 14-in-diameter dome locations, the pressure measurements were made with the heat-flux dome on one side and a flat plate on the other side. The lateral profile skewing is due to the side next to the flat plate having less flow resistance than the side that is adjacent to the heat-flux dome. This nonsymmetric effect is not present for the pressure contours of the 28-in-diameter dome because it was tested singularly without adjacent domes.

Shown in figure 14 are normalized pressure contours and the associated centerline longitudinal distributions for the three flow cases over the highest 14-in-diameter dome. Experimental surface pressure distributions are similar for all three cases. Some slight differences in surface pressure are evident near the forward and aft dome edges for cases 1 and 2 and are probably due to slight differences in the location and extent of separation for the two cases. In general, the pressure gradients over the dome surface for cases 1 and 2 are the same, but case 3 has a larger pressure gradient due to the sharp leading edge producing a boundary layer that has a higher momentum gradient, as can be seen by comparing figures 8(a) and 8(b) with figure 9(a).

The normalized pressure distribution calculated by using the 2-D linearized, small-perturbation theory given by reference 21 is also included in figure 14. Note that the experimental pressure data are in excellent agreement with the pressures as predicted by the 2-D linearized-flow theory with the exception of

the values at the forward and aft edges. The predicted edge pressures disagree with the experimental results because of the velocity gradient through the boundary layer that is not accounted for by the potential-flow theory, 3-D effects of the dome geometry, and forward and aft shock systems generated by flow separation, as described before and illustrated by the inset in figure 10. The actual pressure levels given by the experimental data show good agreement with prediction for both the laminar and the turbulent blunt-leading-edge cases; but for the turbulent sharp-leading-edge case, experimental data are higher than prediction for the 2-D linearized-flow theory, an effect possibly due to a stronger forward shock system or the normalizing factor. However, it is important to note that the longitudinal centerline pressure gradient is being predicted well for all three flow cases by the 2-D linearized theory.

A composite of the normalized longitudinal pressure distribution plots for the three different flow cases is presented as figure 15 in which each plot shows the effect of height variation for a fixed dome diameter. The region of peak longitudinal centerline pressure moves forward and the pressure gradient increases as the dome height is increased at a constant diameter. Stronger shock systems are generated as the dome height increases which cause a greater static pressure rise and the increase of a pressure gradient over the dome. Also, the pressure at the dome center expands back to the flat-plate pressure for most H/D combinations. Note that for the case 1 dome (7-in-diameter), the surface pressure approaches the flat-plate level for increasing x/R (downstream pressure recovery), an effect which suggests that a flow separation shock system may be present on the leeward surface of the dome at $x/R \approx 1.8$ as indicated in figure 15(a). The spanwise effect of this flow separation is shown by the contour plot of this case in figure 13(a) for $D = 7$ in. at $H/D = 0.028$.

Surface Heating-Rate Distribution

Dome heating rates, normalized to the flat-plate reference heating rate for each run, are presented in table V for each flow condition. As indicated earlier, the smaller diameter domes were tested with a triple dome configuration with the heat-flux dome in the center. To establish the effect of the adjacent dome on the surface heating rate, run 6 was made with the single dome for a direct comparison with run 10 which had the triple dome configuration. The results are presented in figure 16 where longitudinal and lateral centerline plots are shown. In general, the heating-rate trends of both the single and triple dome configurations agree quite well except at the lateral

edges, as shown by figure 16(b), where the heating rate for the single dome configuration is above that of the triple dome configuration. As indicated earlier, the lateral-edge pressure was less with no adjacent domes; however, the lateral-edge heating is increased with no adjacent domes because of the increased shear flow. Therefore, the primary variance between the single and triple configurations is limited to a localized region between adjacent domes.

An overview of the heating rates for the three flow cases is given as contour plots in figure 17. This figure presents heating-rate contours with the dome height increasing left to right and the dome diameter increasing top to bottom for the three flow cases. The baseline dome heating-rate contours show little variation in heating rates over the dome surface as was seen with baseline pressure contours, an indication of minimal heat load augmentation for bowed TPS concepts. However, for each flow case as the height of the dome is increased, the location of the peak heating rate shifts forward on the windward side of the dome and the heating-rate gradient increases. Heating contours generally defined peak heating along the windward symmetry line. The nonsymmetric hot spots could have been produced by a time-dependent variation in the test flow field.

Heating-rate longitudinal distributions along with the corresponding contour plots for the 14-in-diameter dome with a nominal height of 0.4 in. are presented in figure 18 for each flow case. The figure shows the boundary-layer effects on the heating rate over the dome. A general comparison between the three flow types shows that the heating-rate gradient is more severe for the turbulent boundary layer with a sharp leading edge than for both blunt-leading-edge flow cases. The peak heating-rate level for the turbulent boundary layer with a sharp leading edge is more than twice the flat-plate level (see fig. 18(c)); whereas for both blunt-leading-edge flow cases, the heating-rate gradient is more gradual and the level of peak heating rate is approximately 1.85 times the flat-plate value for the laminar condition and about 1.70 times the flat-plate value for the turbulent condition. (See figs. 18(a) and 18(b).) A comparison of dome heating rates between the turbulent-boundary-layer flow (cases 2 and 3) and the laminar-boundary-layer flow (case 1) shows that turbulent heating rates fall below the flat-plate reference level on the dome leeward surface, but the laminar heating rate stays above the reference level over most of the dome. Also, the turbulent heating rate for cases 2 and 3 are only slightly larger than the flat-plate heating-rate value at the dome center, and the overall longitudinal distribution is similar to the pressure distributions

presented earlier. The heating rates above the flat-plate value over both the windward and leeward sides of the dome for case 1 (see fig. 18(a)) indicate that transitional effects may be influencing leeward dome heating rates.

A composite of all normalized longitudinal heating-rate distributions is given as figure 19 for the three flow cases. The data of figure 19 are presented as plots of constant dome diameter with a variation in H/D. Normalized heating rates for the laminar boundary layer with blunt leading edge, as presented in figure 19(a), show that peak heating moves both forward and to a higher level as the dome height and/or diameter is increased; and as the dome height increases at a constant diameter, the forward- and aft-edge heating is reduced, especially for the data of the smaller diameter domes. The decrease in edge heating with increased height is believed due to the increased size of the separated-flow regions, illustrated in the inset in figure 10. The forward shift in peak heating with increased dome height and diameter was due in part to the corresponding shift in the reattachment location.

Shown as figure 19(b) and 19(c) are the normalized heating rates for the turbulent boundary layer, case 2 and case 3, respectively. The data trend shows that as height and/or diameter increases, the point of peak heating again shifts forward and heating-rate gradients become larger and are approximately the flat-plate reference value at the dome center. Note that the forward-edge heating rate does not drop below the flat-plate level as with case 1, but the leeward dome heating rate drops below the flat-plate level similar to the corresponding pressure distributions.

Ceramic Dome Temperature

Figure 20 shows temperature contours and a longitudinal centerline temperature distribution for both the laminar and turbulent boundary layer with a blunt leading edge (case 1 and case 2, respectively) over the 7-in-diameter, 0.2-in-height ceramic dome. These measurements were obtained from the overhead infrared camera after a 40-sec exposure time when the surface temperatures had reached a steady state. A comparison between the two cases shows that laminar-flow temperature levels were less than the turbulent-flow levels and that the peak temperature location shifted forward substantially for a turbulent boundary layer. Even though no quantitative heating-rate data were obtained from the infrared temperature time histories, the isotherm patterns of figure 20 are similar to the heating contours shown in figures 17(a) and 17(b).

Augmented Pressure and Heating Rate Over Flat-Plate Values

The pressure and heating-rate distributions obtained in the present tests form a data base to be used in assessing the aerothermal load augmentation of various dome protuberances. For this paper, the increased loads for the 14-in-diameter domes were computed and are presented in this section.

Shown as figure 21 are plots of the normalized peak surface pressure along the longitudinal centerline on the 14-in-diameter pressure dome as a function of dome height for the three flow cases. The symbols show the experimental data and the faired lines are a least-squares linear curve fit for each case. The variation of peak pressure with dome height for cases 1 and 2 is nearly the same, but the peak pressure for case 3 is much greater. The flow of cases 1 and 2 was associated with the blunt leading edge that produced higher entropy gradient flow than the flow of case 3. Therefore, a greater static pressure recovery is possible for case 3 because more flow energy is available in the boundary layer because of lower entropy flow.

Peak normalized heating rate along the longitudinal centerline of the 14-in-diameter dome is plotted against dome height in figure 22 for the three flow cases. The variation of peak heating with dome height is similar to that of the pressure. Although the peak heating of case 1 was greater than that of case 2, the increase in heating with increase in dome height was nearly the same. The heating-rate increase in the case 3 flow is greater than that of the other two cases because the case 3 flow has a more energetic boundary layer near the wall and, therefore, a greater kinetic energy recovery in the form of wall heating.

The extent of heat load augmentation is shown in figure 23 where the absolute and normalized integrated heat load on the 14-in-diameter dome is plotted as a function of dome height. The absolute integrated heat load is presented as a function of dome height in figure 23(a) where case 3 is shown to have the highest heat load, followed by case 2 and lastly by case 1. The normalized heat loads presented in figure 23(b) for the laminar-boundary-layer case show that the augmented heat load increases from 10 to 30 percent with increasing dome height. At the larger dome heights, the augmented heat load for the laminar boundary layer is higher than that for either the blunt or sharp leading edge in a turbulent boundary layer. The higher heat loads for the laminar boundary layer are probably due to transitional effects occurring for the larger dome heights that are not accounted for by the laminar normalizing factor. Blunt

and sharp leading edges in turbulent flow have nearly the same slope, but the level of normalized heat load for the turbulent blunt-leading-edge case is greater, an effect possibly due to a turbulence increase for the blunt-leading-edge turbulent boundary layer as it encounters the dome. The heat load augmentation shown indicates that for the TPS with bowed heights of 0.1 in. or less (the maximum practical bowed heights expected for the TPS), the heat load penalties are no greater than approximately 14 percent for either the laminar or turbulent boundary layers.

Concluding Remarks

Aerothermal tests were conducted in the Langley 8-Foot High-Temperature Tunnel (8' HTT) at a Mach number of 6.5 on a series of spherical dome protuberances mounted on a flat-plate test apparatus. Detailed surface pressure and heating-rate distributions were obtained for dome heights of 0.1, 0.2, 0.4, and 0.8 in. and diameters of 7, 14, and 28 in. submerged in both laminar and turbulent boundary layers. A dome with a height of 0.1 in. and a diameter of 14 in. is representative of a thermally bowed metallic thermal protection system (TPS) tile. Tests were made at a nominal total temperature of 3300°R and a Reynolds number of 0.3×10^6 per foot. The experimental results form a data base that can be used to predict aerothermal load augmentation from dome protuberances typical of bowed TPS tiles.

The present results indicated that for most of the dome heights tested, the flow profile obtained from the pitot probe in the wake region was not significantly affected by the presence of the dome. The large dome heights caused a decrease in Mach number outside the boundary layer from shock losses, and there was some indication of flow transition at the edge of the boundary layer. The surface pressures on the domes were increased on the windward surface and reduced on the leeward surface as predicted by linearized small-perturbation theory, and the distributions were only moderately affected by boundary-layer variations. Surface heating rates increased on the windward surface and decreased on the leeward surface similar to the pressure for turbulent flow; but for laminar boundary layers, the heating rates remained high on the leeward surface, an effect probably due to local transition. Peak windward heating rates increased and moved forward with increasing dome height. Because of transitional flow effects, the heat load augmentation was increased by 30 percent for the maximum dome height in a laminar boundary layer. However, the corresponding augmentation for a dome with a height of 0.1 in. and a diameter of 14 in. representative of a bowed TPS tile was

14 percent or less for either a laminar or a turbulent boundary layer.

NASA Langley Research Center
Hampton, Virginia 23665-5225
October 24, 1986

References

1. Bohon, Herman L.; Sawyer, J. Wayne; Hunt, L. Roane; and Weinstein, Irving: Performance of Full Size Metallic and RSI Thermal Protection Systems in a Mach 7 Environment. AIAA Paper No. 75-800, May 1975.

2. Deveikis, William D.; Miserentino, Robert; Weinstein, Irving; and Shideler, John L.: *Aerothermal Performance and Structural Integrity of a René 41 Thermal Protection System at Mach 6.6.* NASA TN D-7943, 1975.

3. Sawyer, James Wayne: *Aerothermal and Structural Performance of a Cobalt-Base Superalloy Thermal Protection System at Mach 6.6.* NASA TN D-8415, 1977.

4. Bohon, Herman L.; Shideler, John L.; and Rummler, Donald R.: Radiative Metallic Thermal Protection Systems: A Status Report. *J. Spacecr. & Rockets,* vol. 14, no. 10, Oct. 1977, pp. 626–631.

5. Jackson, L. Robert; and Dixon, Sidney C.: *A Design Assessment of Multiwall, Metallic Stand-Off, and RSI Reusable Thermal Protection Systems Including Space Shuttle Application.* NASA TM-81780, 1980.

6. Kelly, H. Neale; and Webb, Granville L.: Assessment of Alternate Thermal Protection Systems for the Space Shuttle Orbiter. AIAA-82-0899, June 1982.

7. Sawyer, James Wayne: *Pressure and Heating-Rate Distributions on a Corrugated Surface in a Supersonic Turbulent Boundary Layer.* NASA TP-1024, 1977.

8. Polak, A.; Werle, M. J.; Vatsa, V. N.; and Bertke, S. D.: Numerical Study of Separated Laminar Boundary Layers Over Multiple Sine-Wave Protuberances. *J. Spacecr. & Rockets,* vol. 13, no. 3, Mar. 1976, pp. 168–173.

9. Yates, John E.: *Linearized Integral Theory of the Viscous Compressible Flow Past a Wavy Wall.* AFOSR-TR-72-1335, U.S. Air Force, July 1972. (Available from DTIC as AD 746 332.)

10. Brandon, H. J.; and Masek, R. V.: *Measurement and Correlation of Aerodynamic Heating to Surface Corrugation Stiffened Structures in Thick Turbulent Boundary Layers.* NASA CR-132503, [1974].

11. Olsen, George C.; and Smith, R. E.: Analysis of Aerothermal Loads on Spherical Dome Protuberances. AIAA-83-1557, June 1983.

12. Olsen, George C.; and Smith, R. E.: Aerothermal Loads Analysis for High Speed Flow Over a Quilted Surface Configuration. AIAA-84-1630, June 1984.

13. Deveikis, William D.; and Hunt, L. Roane: *Loading and Heating of a Large Flat Plate at Mach 7 in the Langley 8-Foot High-Temperature Structures Tunnel.* NASA TN D-7275, 1973.

14. Deveikis, William D.; Bruce, Walter E., Jr.; and Karns, John R.: *Techniques for Aerothermal Tests of Large,*

Flightweight Thermal Protection Panels in a Mach 7 Wind Tunnel. NASA TM X-71983, 1974.

15. Leyhe, E. W.; and Howell, R. R.: *Calculation Procedure for Thermodynamic, Transport, and Flow Properties of the Combustion Products of a Hydrocarbon Fuel Mixture Burned in Air With Results for Ethylene-Air and Methane-Air Mixtures.* NASA TN D-914, 1962.

16. Harris, Julius E.; and Blanchard, Doris K.: *Computer Program for Solving Laminar, Transitional, or Turbulent Compressible Boundary-Layer Equations for Two-Dimensional and Axisymmetric Flow.* NASA TM-83207, 1981.

17. White, Frank M.: *Viscous Fluid Flow.* McGraw-Hill, Inc., 1974, p. 493.

18. Ames Research Staff: *Equations, Tables, and Charts for Compressible Flow.* NACA Rep. 1135, 1953. (Supersedes NACA TN 1428.)

19. Bushnell, Dennis M.; Johnson, Charles B.; Harvey, William D.; and Feller, William V.: *Comparison of Prediction Methods and Studies of Relaxation in Hypersonic Turbulent Nozzle-Wall Boundary Layers.* NASA TN D-5433, 1969.

20. Schlichting, Hermann (J. Kestin, transl.): *Boundary-Layer Theory,* Seventh ed. McGraw-Hill Book Co., c.1979, p. 637.

21. Anderson, John D., Jr.: *Modern Compressible Flow— With Historical Perspective.* McGraw-Hill, Inc., c.1982, p. 231.

Table I. Instrument Locations for Both Pressure- and Thermocouple-Instrumented Domes

Location	θ, deg	r/R	Location	θ, deg	r/R
1	0	0.943	30	135.0	0.786
2		.786	31		.629
3		.629	32		.471
4		.471	33		.314
5		.314	34	↓	.157
6		.157	35	157.5	.943
7	↓	0	36	157.5	.629
8	22.5	.943	37	157.5	.314
9	22.5	.629	38	180.0	.943
10	22.5	.314	39		.786
11	45.0	.943	40		.629
12		.786	41		.471
13		.629	42		.314
14		.471	43	↓	.157
15		.314	44	270.0	.943
16	↓	.157	45		.786
17	67.5	.943	46		.629
18	67.5	.629	47		.471
19	67.5	.314	48		.314
20	90.0	.943	49	↓	.157
21		.786	50	292.5	.943
22		.629	51	292.5	.629
23		.471	52	292.5	.314
24		.314	53	315.0	.943
25	↓	.157	54	315.0	.629
26	112.5	.943	55	315.0	.314
27	112.5	.629	56	337.5	.943
28	112.5	.314	57	337.5	.629
29	135.0	.943	58	337.5	.314

Table II. Free-Stream Flow and Model Reference Values

Run	M_∞	$T_{t,\infty}$, °R	$p_{t,\infty}$, psia	p_∞, psia	p_{lp}, psia	p_{fp}, psia	q_{lp}, $\frac{Btu}{ft^2\text{-}sec}$	q_{fp}, $\frac{Btu}{ft^2\text{-}sec}$	D, in.	H_{PD}, in.	H_{TD}, in.	H_{CD}, in.	S_R, in.
						Blunt leading edge without trips							
[a]1	6.55	3370	410	0.095	0.1716	0.1870	0.836	0.657					58.1
[a]2	6.58	3490	400	.087		.1706		.669					89.1
3	6.58	3530	440	.094	.1826	.1815	.896	.749	7.0			0.188	
4	6.57	3480	430	.093	.1742	.1732	.880	.736	7.0			.092	
5	6.62	3700	490	.094	.1868	.1857	.938	.784	7.0			.040	
6	6.59	3540	410	.087	.1741	.1731	.833	.696	14.0		0.455		89.1
7	6.54	3360	400	.092	.1821	.1810	.776	.649	7.0	0.208	.174	.194	89.1
8	6.60	3580	420	.087	.1665	.1655	.842	.704	7.0	.097	.103	.110	89.1
9	6.56	3440	420	.092	.1769	.1758	.817	.683	7.0	.051	.087	.044	89.1
10	6.59	3570	420	.087	.1703	.1693	.883	.738	14.0	.395	.455	.411	89.1
11	6.54	3340	380	.088	.1682	.1672	.846	.707	14.0	.202	.207	.216	89.1
12	6.56	3430	420	.093	.1843	.1832	.764	.639	14.0	.114	.151	.113	89.1
13	6.60	3590	460	.094		.1863		.721	28.0	.785			89.1
14	6.59	3410	420	.094		.1850		.669	28.0		.760		89.1
15	6.61	3630	470	.094		.1870		.715	28.0	.384			89.1
						Blunt leading edge with trips							
[a]16	6.60	3590	460	0.094	0.1853	0.1817	2.402	2.311					58.1
[a]17	6.59	3550	450	.094		.1816		2.280					89.1
18	6.56	3420	420	.094	.1777	.1741	2.369	2.248	7.0			0.188	
19	6.57	3420	420	.092	.1830	.1793	2.186	2.075	7.0	0.195	0.176	188	89.1
20	6.53	3290	390	.092	.1779	.1743	2.069	1.963	7.0	.106	.102	.117	89.1
21	6.56	3420	410	.092	.1817	.1781	2.041	1.937	7.0	.051	.087	.044	89.1
22	6.61	3640	460	.093	.1880	.1842	2.094	1.987	14.0	.398	.457	.400	89.1
23	6.60	3610	460	.095	.1864	.1827	2.214	2.101	14.0	.186	.193	.204	89.1
24	6.60	3620	460	.094	.1825	.1789	2.126	2.018	14.0	.104	.153	.099	89.1
25	6.61	3650	470	.094		.1830		2.331	28.0	.788			89.1
26	6.59	3750	450	.094		.1817		2.423	28.0		.760		89.1
27	6.60	3610	460	.095		.1830		2.321	28.0	.368			89.1

[a]Runs to establish flat-plate correlation.

Table II. Concluded

Run	M_∞	$T_{t,\infty}$, °R	$p_{t,\infty}$, psia	p_∞, psia	p_{ip}, psia	p_{fp}, psia	q_{ip}, $\dfrac{Btu}{ft^2\text{-sec}}$	q_{fp}, $\dfrac{Btu}{ft^2\text{-sec}}$	D, in.	H_{PD}, in.	H_{TD}, in.	H_{CD}, in.	S_R, in.
					Sharp leading edge with trips								
[a]28	6.59	3540	450	0.094		0.1863		3.779					58.1
[a]29	6.57	3490	440	.094	0.1890	.1876	4.929	3.711					89.1
30	6.60	3590	460	.095	.1867	.1854	5.590	4.210	14.0	0.390	0.465	0.401	89.1
31	6.60	3460	430	.094	.1862	.1849	5.570	4.194	14.0	.182	.179	.205	89.1
32	6.60	3530	450	.095	.1869	.1856	5.326	4.010	14.0	.090	.144	.095	89.1
.													
33	6.62	3700	1820	.353	.623	.6590	13.21	10.12					89.1

[a]Runs to establish flat-plate correlation.

Table III. Mach Number Values From Boundary-Layer Probe

Run	M_1 with z = 0.032 in.	M_2 with z = 0.096 in.	M_3 with z = 0.160 in.	M_4 with z = 0.224 in.	M_5 with z = 0.288 in.	M_6 with z = 0.416 in.	M_7 with z = 0.544 in.	M_8 with z = 0.673 in.	M_9 with z = 0.800 in.	M_{10} with z = 0.928 in.	M_{11} with z = 1.12 in.	M_{12} with z = 1.44 in.	M_{13} with z = 2.00 in.	M_{14} with z = 2.50 in.
						BLUNT LEADING EDGE WITHOUT TRIPS								
1	.72	1.18	1.69	2.07	2.31	2.66	2.99	3.07	3.19	3.27	3.48	3.92	4.63	5.19
2	.66	1.15	1.59	1.90	2.06	2.50	2.79	2.92	3.05	3.08	3.38	3.79	4.56	5.08
6	.44	.80	1.44	1.74	2.02	2.55	2.87	2.99	3.15	3.26	3.47	3.86	3.94	4.55
7	.63	1.06	1.50	1.84	2.06	2.51	2.80	2.95	3.10	3.21	3.41	3.80	4.53	4.96
8	.81	1.29	1.62	1.95	2.14	2.56	2.87	3.02	3.19	3.31	3.52	3.93	4.57	4.97
9	.72	1.20	1.59	1.92	2.11	2.54	2.84	2.96	3.10	3.21	3.42	3.82	4.54	4.98
10	.73	1.00	1.17	1.55	1.84	2.38	2.77	2.97	3.15	3.28	3.49	3.90	4.16	4.49
11	.82	1.35	1.62	1.85	2.07	2.51	2.83	2.97	3.14	3.26	3.48	3.89	4.40	4.74
12	.72	1.12	1.49	1.85	2.07	2.50	2.80	2.92	3.06	3.18	3.40	3.80	4.49	4.80
13	.77	1.13	1.64	2.04	2.29	2.70	3.05	3.17	3.34	3.43	3.65	4.02	4.17	4.57
14	.75	1.13	1.60	1.99	2.24	2.67	3.02	3.14	3.29	3.39	3.59	3.91	3.99	4.54
15	.81	1.24	1.70	2.07	2.28	2.67	3.02	3.14	3.30	3.41	3.62	4.04	4.43	4.77
						BLUNT LEADING EDGE WITH TRIPS								
16	1.02	1.63	1.88	2.10	2.23	2.48	2.74	2.85	3.02	3.13	3.36	3.79	4.54	5.02
17	1.30	1.67	2.03	2.12	2.16	2.30	2.47	2.57	2.73	2.87	3.12	3.55	4.43	4.77
19	1.31	1.67	2.02	2.11	2.13	2.30	2.49	2.59	2.76	2.89	3.13	3.55	4.45	4.90
20	1.30	1.86	2.01	2.10	2.16	2.31	2.53	2.62	2.78	2.91	3.13	3.55	4.45	4.96
21	1.26	1.82	1.98	2.09	2.13	2.29	2.48	2.59	2.75	2.88	3.11	3.53	4.40	4.81
22	1.19	1.77	1.96	2.02	2.09	2.27	2.47	2.58	2.75	2.90	3.08	3.55	3.74	4.17
23	1.17	1.76	1.93	2.05	2.11	2.27	2.46	2.57	2.73	2.86	3.10	3.52	4.13	4.55
24	1.18	1.76	1.96	2.07	2.13	2.32	2.54	2.65	2.81	2.95	3.13	3.60	4.36	4.60
25	1.13	1.88	2.09	2.22	2.28	2.44	2.65	2.79	2.96	3.10	3.33	3.73	3.90	4.48
26	1.12	1.89	2.10	2.23	2.29	2.45	2.64	2.78	2.97	3.08	3.30	3.67	3.73	4.37
27	1.15	1.90	2.14	2.19	2.25	2.42	2.62	2.75	2.94	3.07	3.30	3.73	4.31	4.69
						SHARP LEADING EDGE WITH TRIPS								
28	1.75	3.05	3.31	3.44	3.53	3.82	4.37	4.63	5.05	5.42	5.84	6.01	6.03	6.09
29	1.71	2.86	3.08	3.19	3.29	3.54	3.95	4.26	4.54	4.72	5.27	5.79	6.03	6.04
30	1.71	2.91	3.14	3.22	3.33	3.61	4.11	4.33	4.56	4.71	5.08	4.63	5.40	5.96
31	1.69	2.89	3.11	3.21	3.31	3.58	4.01	4.32	4.55	4.72	5.29	5.08	5.77	6.11
32	1.68	2.83	3.10	3.16	3.26	3.52	3.95	4.27	4.57	4.67	5.23	5.36	5.74	5.99
33	2.05	2.99	3.13	3.26	3.41	3.73	4.19	4.51	4.74	5.00	5.75	6.10	6.28	6.21

Table IV. Pressure Values From Pressure-Instrumented Dome

Run	$\dfrac{p_1}{p_{fp}}$	$\dfrac{p_2}{p_{fp}}$	$\dfrac{p_3}{p_{fp}}$	$\dfrac{p_4}{p_{fp}}$	$\dfrac{p_5}{p_{fp}}$	$\dfrac{p_6}{p_{fp}}$	$\dfrac{p_7}{p_{fp}}$	$\dfrac{p_8}{p_{fp}}$	$\dfrac{p_9}{p_{fp}}$	$\dfrac{p_{10}}{p_{fp}}$	$\dfrac{p_{11}}{p_{fp}}$	$\dfrac{p_{12}}{p_{fp}}$
							BLUNT LEADING EDGE WITHOUT TRIPS					
6	.000	.000	.000	.000	.000	.000	.000	.000	.000	.000	.000	.000
7	1.149	1.204	1.199	1.171	1.099	1.022	.983	1.155	1.177	1.105	1.116	1.138
8	1.088	1.094	1.076	1.051	1.021	.979	.973	1.082	1.063	1.027	1.057	1.045
9	1.047	1.052	1.092	1.058	1.035	.995	.995	1.041	1.041	1.035	.995	1.030
10	1.205	1.288	1.294	1.240	1.170	1.099	1.034	1.181	1.258	1.164	1.158	1.187
11	.000	1.118	1.106	1.077	1.023	1.011	.981	1.089	1.094	1.053	1.071	1.071
12	1.021	1.037	1.059	1.026	.999	.988	.983	1.010	1.015	1.010	.988	1.015
13	1.249	1.337	1.326	1.294	1.235	1.165	1.084	1.245	.000	1.224	1.181	1.251
14	.000	.000	.000	.000	.000	.000	.000	.000	.000	.000	.000	.000
15	1.112	1.144	1.144	1.128	1.075	1.064	1.011	1.128	1.118	1.091	1.102	1.096
							BLUNT LEADING EDGE WITH TRIPS					
19	1.260	1.288	1.266	1.177	1.132	1.065	1.021	1.244	1.227	1.149	1.205	1.194
20	1.119	1.113	1.119	1.067	1.038	1.021	.998	1.102	1.096	1.044	1.073	1.073
21	1.050	1.044	1.072	1.095	1.050	.999	1.016	1.056	1.044	1.067	1.016	1.022
22	1.265	1.303	1.306	1.276	1.129	1.113	1.021	1.243	1.260	1.151	1.205	1.216
23	1.100	1.095	1.128	1.073	1.040	1.024	.991	1.078	1.095	1.040	1.056	1.067
24	1.051	1.051	1.084	1.079	1.023	1.006	.989	1.034	1.034	1.051	1.006	1.029
25	1.328	1.372	1.355	1.333	1.268	1.202	1.115	1.311	.000	1.262	1.246	1.284
26	.000	.000	.000	.000	.000	.000	.000	.000	.000	.000	.000	.000
27	1.120	1.137	1.153	1.126	1.093	1.087	1.060	1.153	1.153	1.109	1.109	1.104
							SHARP LEADING EDGE WITH TRIPS					
30	1.435	1.516	1.499	1.446	1.321	1.219	1.106	1.408	1.456	1.348	1.338	1.359
31	1.179	1.201	1.206	1.157	1.076	1.087	1.033	1.157	1.179	1.103	1.130	1.157
32	1.083	1.115	1.137	1.099	1.072	1.051	1.029	1.083	1.083	1.061	1.072	1.056

Table IV. Continued

Run	$\frac{p_{13}}{p_{fp}}$	$\frac{p_{14}}{p_{fp}}$	$\frac{p_{15}}{p_{fp}}$	$\frac{p_{16}}{p_{fp}}$	$\frac{p_{17}}{p_{fp}}$	$\frac{p_{18}}{p_{fp}}$	$\frac{p_{19}}{p_{fp}}$	$\frac{p_{20}}{p_{fp}}$	$\frac{p_{21}}{p_{fp}}$	$\frac{p_{22}}{p_{fp}}$	$\frac{p_{23}}{p_{fp}}$	$\frac{p_{24}}{p_{fp}}$
						BLUNT LEADING EDGE WITHOUT TRIPS						
6	.000	.000	.000	.000	.000	.000	.000	.000	.000	.000	.000	.000
7	1.127	1.099	1.055	.989	1.088	1.061	1.017	.000	1.000	.989	.983	.978
8	1.033	1.021	1.009	.997	1.069	1.015	.985	.000	.955	.991	1.003	.997
9	1.047	1.047	1.030	.984	1.018	1.001	1.001	.000	.990	1.013	1.007	1.030
10	1.199	1.170	1.116	1.063	1.170	1.110	1.081	.000	1.057	1.045	1.028	1.034
11	1.071	1.047	1.029	1.005	1.077	1.029	1.011	.000	1.011	1.005	.999	.981
12	1.004	.999	.993	.966	1.015	.988	.977	.000	.977	.977	.972	.977
13	1.251	1.224	1.186	1.122	1.090	1.138	1.138	.000	.998	1.025	1.041	1.100
14	.000	.000	.000	.000	.000	.000	.000	.000	.000	.000	.000	.000
15	1.091	1.086	1.053	1.021	1.037	1.037	1.037	.000	.963	.968	.995	1.011
						BLUNT LEADING EDGE WITH TRIPS						
19	1.177	1.132	1.093	1.037	1.143	1.104	1.060	.000	1.026	.993	1.021	1.021
20	1.067	1.050	1.027	.970	1.050	1.021	1.010	.000	.987	.987	.993	.998
21	1.028	1.039	1.028	.977	1.022	1.011	1.005	.000	.988	1.005	1.005	.994
22	1.211	1.140	1.140	1.053	1.173	1.118	1.097	.000	1.042	1.048	1.037	1.042
23	1.073	1.056	1.034	1.002	1.062	1.029	1.007	.000	1.007	.980	1.002	1.002
24	1.029	1.017	1.017	.989	1.034	1.006	1.006	.000	.995	.961	1.006	1.012
25	1.279	1.262	1.219	1.158	1.158	1.175	1.175	.000	1.027	1.055	1.066	1.109
26	.000	.000	.000	.000	.000	.000	.000	.000	.000	.000	.000	.000
27	1.104	1.109	1.087	1.055	1.071	1.049	1.033	.000	1.000	1.005	1.027	1.044
						SHARP LEADING EDGE WITH TRIPS						
30	1.348	1.316	1.251	1.160	1.214	1.214	1.181	.000	1.025	1.068	1.095	1.100
31	1.154	1.114	1.098	1.060	1.103	1.087	1.071	.000	1.017	1.033	1.038	1.060
32	1.061	1.051	1.040	1.018	1.051	1.034	1.024	.000	.997	1.068	1.018	1.024

16

Table IV. Continued

Run	$\frac{p_{25}}{p_{fp}}$	$\frac{p_{26}}{p_{fp}}$	$\frac{p_{27}}{p_{fp}}$	$\frac{p_{28}}{p_{fp}}$	$\frac{p_{29}}{p_{fp}}$	$\frac{p_{30}}{p_{fp}}$	$\frac{p_{31}}{p_{fp}}$	$\frac{p_{32}}{p_{fp}}$	$\frac{p_{33}}{p_{fp}}$	$\frac{p_{34}}{p_{fp}}$	$\frac{p_{35}}{p_{fp}}$	$\frac{p_{36}}{p_{fp}}$
BLUNT LEADING EDGE WITHOUT TRIPS												
6	.000	.000	.000	.000	.000	.000	.000	.000	.000	.000	.000	.000
7	.972	.923	.912	.928	.878	.816	.757	.873	.895	.934	.856	.768
8	.979	.949	.937	.943	.918	.894	.894	.924	.931	.943	.894	.864
9	.995	1.001	.978	.973	.990	.973	.967	.967	.967	.978	.939	.950
10	1.034	.969	.951	.975	.874	.827	.845	.886	.933	.981	.774	.768
11	.987	.981	.957	.963	.903	.915	.915	.927	.951	.975	.831	.873
12	.972	.972	.955	.955	.944	.928	.939	.944	.955	.961	.917	.906
13	1.074	.886	.907	.993	.768	.751	.811	.875	.955	1.020	.676	.746
14	.000	.000	.000	.000	.000	.000	.000	.000	.000	.000	.000	.000
15	1.016	.914	.920	.979	.856	.840	.877	.920	.963	.984	.770	.845
BLUNT LEADING EDGE WITH TRIPS												
19	1.015	.987	.937	.959	.870	.853	.859	.892	.931	.970	.820	.803
20	.993	.987	.000	.964	.924	.906	.918	.941	.952	.970	.866	.872
21	.983	1.022	.977	.966	.999	.938	.966	.971	.966	.988	.932	.949
22	1.053	.999	.945	.995	.890	.852	.858	.896	.945	.993	.717	.787
23	.996	.991	.000	.969	.930	.909	.920	.925	.958	.974	.832	.876
24	.989	1.012	.961	.978	.973	.956	.950	.961	.973	.984	.911	.928
25	.000	.091	.934	1.033	.732	.770	.836	.918	.989	1.049	.634	.776
26	.000	.000	.000	.000	.000	.000	.000	.000	.000	.000	.000	.000
27	1.044	.923	.951	1.011	.847	.869	.907	.945	1.000	1.016	.798	.874
SHARP LEADING EDGE WITH TRIPS												
30	1.106	.960	.928	1.019	.728	.750	.804	.885	.955	1.030	.593	.734
31	1.038	.990	.968	1.006	.860	.892	.909	.936	.979	1.011	.790	.865
32	1.002	1.062	.975	.991	.921	.954	.943	.959	.975	.997	.873	.916

17

Table IV. Continued

Run	$\dfrac{p_{37}}{p_{fp}}$	$\dfrac{p_{38}}{p_{fp}}$	$\dfrac{p_{39}}{p_{fp}}$	$\dfrac{p_{40}}{p_{fp}}$	$\dfrac{p_{41}}{p_{fp}}$	$\dfrac{p_{42}}{p_{fp}}$	$\dfrac{p_{43}}{p_{fp}}$	$\dfrac{p_{44}}{p_{fp}}$	$\dfrac{p_{45}}{p_{fp}}$	$\dfrac{p_{46}}{p_{fp}}$	$\dfrac{p_{47}}{p_{fp}}$	$\dfrac{p_{48}}{p_{fp}}$
BLUNT LEADING EDGE WITHOUT TRIPS												
6	.000	.000	.000	.000	.000	.000	.000	.000	.000	.000	.000	.000
7	.851	.862	.762	.757	.796	.851	.912	.967	.972	.967	.967	.967
8	.912	.866	.834	.852	.882	.906	.943	.973	.967	.967	.967	.931
9	.956	.939	.939	.927	.950	.950	.978	.973	1.001	1.001	.995	.984
10	.898	.679	.679	.738	.821	.880	.951	.957	.969	.992	.998	1.022
11	.945	.789	.825	.855	.891	.921	.951	.921	.945	.963	.969	.951
12	.939	.679	.879	.901	.906	.939	.966	.917	.939	.966	.950	.961
13	.918	.633	.644	.725	.811	.902	.988	.982	.998	1.025	1.036	1.063
14	.000	.000	.000	.000	.000	.000	.000	.000	.000	.000	.000	.000
15	.936	.743	.791	.834	.888	.947	.973	.947	.968	.957	.989	.989
BLUNT LEADING EDGE WITH TRIPS												
19	.698	.753	.731	.786	.831	.887	.954	.982	1.009	1.015	1.015	1.009
20	.935	.632	.849	.878	.906	.912	.958	.981	.981	.987	.987	.987
21	.949	.921	.932	.938	.943	.949	.977	.983	1.005	.983	1.005	.994
22	.912	.635	.689	.765	.825	.896	.966	.945	.966	.934	1.015	1.010
23	.930	.768	.826	.859	.881	.925	.958	.914	.930	.952	.963	.980
24	.961	.883	.900	.917	.959	.956	.973	.922	.939	.967	.978	.984
25	.945	.601	.672	.760	.847	.940	1.022	1.027	1.038	1.027	1.044	1.093
26	.000	.000	.000	.000	.000	.000	.000	.000	.000	.000	.000	.000
27	.973	.760	.825	.874	.940	.973	1.005	.978	.989	.995	1.016	1.016
SHARP LEADING EDGE WITH TRIPS												
30	.906	.561	.620	.712	.820	.895	.998	.944	1.052	1.079	1.036	1.117
31	.956	.763	.817	.855	.903	.952	1.001	.941	1.006	1.028	1.028	1.049
32	.938	.867	.900	.911	.948	.970	.997	.938	1.008	1.018	1.018	.997

Table IV. Concluded

Run	$\frac{p_{49}}{p_{fp}}$	$\frac{p_{50}}{p_{fp}}$	$\frac{p_{51}}{p_{fp}}$	$\frac{p_{52}}{p_{fp}}$	$\frac{p_{53}}{p_{fp}}$	$\frac{p_{54}}{p_{fp}}$	$\frac{p_{55}}{p_{fp}}$	$\frac{p_{56}}{p_{fp}}$	$\frac{p_{57}}{p_{fp}}$	$\frac{p_{58}}{p_{fp}}$
					BLUNT LEADING EDGE WITHOUT TRIPS					
6	.000	.000	.000	.000	.000	.000	.000	.000	.000	.000
7	.950	1.033	1.044	1.017	1.099	1.116	1.066	1.144	1.177	1.083
8	.961	.997	1.009	.991	1.051	1.039	1.021	1.106	1.076	1.045
9	.961	1.013	1.024	.973	1.024	1.035	1.024	1.035	1.052	1.035
10	1.022	1.069	1.105	1.081	1.164	1.199	1.140	1.217	1.264	1.164
11	.981	.993	1.005	1.005	1.035	1.053	1.035	1.160	1.089	1.100
12	.950	.950	.972	.939	1.004	.999	.999	1.026	1.015	1.004
13	1.068	1.079	1.133	1.122	1.154	1.235	1.192	1.202	1.310	1.224
14	.000	.000	.000	.000	.000	.000	.000	.000	.000	.000
15	1.011	1.011	1.027	1.027	1.059	1.075	1.064	1.091	1.118	1.070
					BLUNT LEADING EDGE WITH TRIPS					
19	1.009	1.115	1.093	1.060	1.188	1.171	1.104	1.238	1.227	1.132
20	.981	1.038	1.027	.981	1.079	1.056	1.033	1.102	1.119	1.044
21	.966	1.022	1.028	1.011	1.033	1.033	1.039	1.044	1.050	1.050
22	1.037	1.080	1.102	1.086	1.194	1.194	1.135	1.270	1.270	1.173
23	.958	.991	1.007	1.002	1.051	1.007	1.034	1.089	1.084	1.045
24	.973	.973	.989	.956	1.023	1.017	1.012	1.062	1.045	1.023
25	1.104	1.148	1.180	1.164	1.240	1.279	1.235	1.284	1.355	1.268
26	.000	.000	.000	.000	.000	.000	.000	.000	.000	.000
27	1.027	1.027	1.035	1.049	1.077	1.093	1.082	1.115	1.131	1.115
					SHARP LEADING EDGE WITH TRIPS					
30	1.106	1.197	1.241	1.192	1.343	1.375	1.273	1.440	1.467	1.305
31	1.026	1.076	1.098	1.082	1.141	1.163	1.114	1.195	1.195	1.136
32	1.018	1.040	1.056	1.045	1.088	1.088	1.061	1.115	1.105	1.061

19

Table V. Heating-Rate Values From Thermocouple-Instrumented Heat-Flux Dome

Run	$\frac{q_1}{q_{fp}}$	$\frac{q_2}{q_{fp}}$	$\frac{q_3}{q_{fp}}$	$\frac{q_4}{q_{fp}}$	$\frac{q_5}{q_{fp}}$	$\frac{q_6}{q_{fp}}$	$\frac{q_7}{q_{fp}}$	$\frac{q_8}{q_{fp}}$	$\frac{q_9}{q_{fp}}$	$\frac{q_{10}}{q_{fp}}$	$\frac{q_{11}}{q_{fp}}$	$\frac{q_{12}}{q_{fp}}$
					BLUNT LEADING EDGE WITHOUT TRIPS							
6	.761	1.613	1.884	1.935	1.916	1.807	1.608	.815	1.907	2.000	1.038	1.694
7	.600	1.210	1.431	1.530	1.515	1.436	1.323	1.006	1.436	1.541	.868	1.099
8	.725	1.193	1.132	1.126	1.208	1.166	1.140	.657	1.194	1.260	.683	1.105
9	.777	1.032	1.120	1.115	1.175	1.234	1.199	.827	1.127	1.239	.759	.980
10	.759	1.555	1.799	1.850	1.825	1.684	1.511	.838	1.842	1.898	.986	1.639
11	1.001	1.127	1.294	1.305	1.323	1.294	1.283	1.042	1.171	1.282	.962	1.165
12	1.382	1.102	1.102	1.220	1.273	1.326	1.296	.911	1.115	1.324	1.245	1.120
13	.000	.000	.000	.000	.000	.000	.000	.000	.000	.000	.000	.000
14	1.288	2.052	1.978	1.826	1.722	1.576	1.586	1.327	1.961	1.729	1.622	2.255
15	.000	.000	.000	.000	.000	.000	.000	.000	.000	.000	.000	.000
					BLUNT LEADING EDGE WITH TRIPS							
19	1.044	1.246	1.264	1.162	1.094	1.007	.915	1.166	1.261	1.130	1.076	1.207
20	.993	1.444	1.109	1.069	1.078	1.036	.997	.916	1.148	1.108	.983	1.163
21	.998	1.116	1.179	1.113	1.132	1.122	1.048	1.010	1.176	1.153	.958	1.124
22	1.194	1.037	1.595	1.476	1.388	1.284	1.162	1.425	1.714	1.423	1.674	1.801
23	1.116	1.173	1.153	1.121	1.098	1.075	1.063	1.234	1.205	1.128	1.296	1.331
24	1.173	1.069	1.090	1.139	1.139	1.124	1.069	1.062	1.169	1.169	1.352	1.273
25	.000	.000	.000	.000	.000	.000	.000	.000	.000	.000	.000	.000
26	1.152	1.323	1.257	1.143	1.052	1.024	1.006	1.486	1.439	1.181	1.703	1.610
27	.000	.000	.000	.000	.000	.000	.000	.000	.000	.000	.000	.000
					SHARP LEADING EDGE WITH TRIPS							
30	1.564	1.994	1.776	1.574	1.380	1.253	1.101	1.620	1.745	1.366	1.766	1.686
31	1.376	1.316	.000	1.161	1.125	1.085	1.047	1.368	1.221	1.125	1.216	1.238
32	1.316	1.177	1.230	1.223	1.171	1.107	1.010	1.115	1.242	1.169	1.290	1.189

Table V. Continued

Run	$\frac{q_{13}}{q_{fp}}$	$\frac{q_{14}}{q_{fp}}$	$\frac{q_{15}}{q_{fp}}$	$\frac{q_{16}}{q_{fp}}$	$\frac{q_{17}}{q_{fp}}$	$\frac{q_{18}}{q_{fp}}$	$\frac{q_{19}}{q_{fp}}$	$\frac{q_{20}}{q_{fp}}$	$\frac{q_{21}}{q_{fp}}$	$\frac{q_{22}}{q_{fp}}$	$\frac{q_{23}}{q_{fp}}$	$\frac{q_{24}}{q_{fp}}$
					BLUNT LEADING EDGE WITHOUT TRIPS							
6	1.920	1.979	1.921	1.783	.944	1.808	1.824	1.178	1.743	1.729	1.760	1.665
7	1.386	1.536	1.533	1.454	.639	1.368	1.502	.732	.999	1.271	1.363	1.433
8	1.175	1.143	1.238	1.195	.705	1.174	1.234	.683	1.032	1.133	1.195	1.180
9	1.069	1.153	1.236	1.254	.579	1.085	1.296	.670	.981	1.090	1.138	1.157
10	1.819	1.888	1.839	1.707	.654	1.697	1.723	.701	1.548	1.604	1.623	1.594
11	1.223	1.289	1.259	1.245	.913	1.221	1.281	.819	1.053	1.130	1.177	1.178
12	1.084	1.195	1.259	1.323	.943	1.159	1.251	.740	1.058	1.105	1.131	1.205
13	.000	.000	.000	.000	.000	.000	.000	.000	.000	.000	.000	.000
14	2.164	1.860	1.772	1.613	1.818	1.983	1.856	2.108	2.034	1.989	1.941	1.712
15	.000	.000	.000	.000	.000	.000	.000	.000	.000	.000	.000	.000
					BLUNT LEADING EDGE WITH TRIPS							
19	1.175	1.209	1.087	1.021	.958	1.111	1.073	.994	1.014	1.061	1.004	1.063
20	1.133	1.077	1.090	1.045	.982	.000	1.090	1.000	1.066	1.053	1.045	1.028
21	1.161	1.175	1.166	1.120	.904	1.171	1.160	.961	1.107	1.104	1.097	1.066
22	1.089	1.248	1.405	1.290	1.466	1.525	1.339	1.541	1.435	1.380	1.309	1.255
23	1.266	1.220	1.153	1.089	1.340	1.269	1.141	1.288	1.222	1.210	1.165	1.108
24	1.224	1.243	1.198	1.114	1.282	1.264	1.176	1.248	1.285	1.242	1.203	1.145
25	.000	.000	.000	.000	.000	.000	.000	.000	.000	.000	.000	.000
26	1.506	1.310	1.227	1.109	1.607	1.332	1.270	1.344	1.360	1.315	1.269	1.128
27	.000	.000	.000	.000	.000	.000	.000	.000	.000	.000	.000	.000
					SHARP LEADING EDGE WITH TRIPS							
30	1.593	1.422	1.309	1.185	1.278	1.341	1.188	1.240	1.160	1.144	1.120	1.055
31	1.176	1.139	1.104	1.064	1.144	1.112	1.079	1.030	1.007	1.023	1.018	1.020
32	1.159	1.178	1.139	1.052	1.038	1.105	1.076	1.045	1.010	1.015	1.011	1.008

Table V. Continued

Run	$\dfrac{q_{25}}{q_{fp}}$	$\dfrac{q_{26}}{q_{fp}}$	$\dfrac{q_{27}}{q_{fp}}$	$\dfrac{q_{28}}{q_{fp}}$	$\dfrac{q_{29}}{q_{fp}}$	$\dfrac{q_{30}}{q_{fp}}$	$\dfrac{q_{31}}{q_{fp}}$	$\dfrac{q_{32}}{q_{fp}}$	$\dfrac{q_{33}}{q_{fp}}$	$\dfrac{q_{34}}{q_{fp}}$	$\dfrac{q_{35}}{q_{fp}}$	$\dfrac{q_{36}}{q_{fp}}$
				BLUNT	LEADING	EDGE	WITHOUT	TRIPS				
6	1.560	1.161	1.546	1.543	.986	1.355	1.401	1.470	1.501	1.566	.611	1.385
7	1.327	.572	1.223	1.340	.711	1.005	1.123	1.280	1.334	1.367	.553	1.126
8	1.199	.703	1.063	1.190	.750	1.051	1.055	1.163	1.205	1.205	.683	1.080
9	1.250	.685	1.057	1.227	.729	.970	1.017	1.131	1.195	1.236	.732	1.061
10	1.555	.937	1.424	1.518	1.003	1.195	1.374	1.410	1.449	1.469	.535	1.286
11	1.226	.917	1.097	1.206	.796	1.031	1.101	1.124	1.250	1.213	.760	1.102
12	1.183	1.013	1.086	1.223	1.017	1.051	1.091	1.156	1.181	1.210	1.076	1.094
13	.000	.000	.000	.000	.000	.000	.000	.000	.000	.000	.000	.000
14	1.585	1.682	1.782	1.646	1.009	1.435	1.481	1.541	1.583	1.581	.893	1.414
15	.000	.000	.000	.000	.000	.000	.000	.000	.000	.000	.000	.000
				BLUNT	LEADING	EDGE	WITH	TRIPS				
19	1.013	.895	.948	.956	.710	.819	.823	.886	.851	.920	.539	.772
20	1.026	.879	.948	1.000	.787	.918	.905	.963	.984	.984	.738	.891
21	1.034	.956	1.080	1.058	.878	.985	.981	1.011	1.021	1.044	.839	.935
22	1.125	1.167	1.156	1.182	.952	.972	1.049	1.100	1.131	1.136	.700	.957
23	1.085	1.190	1.127	1.095	.992	1.036	1.045	1.063	1.065	1.051	.880	.988
24	1.075	1.301	1.175	1.103	1.167	1.126	1.083	1.086	1.042	1.045	1.052	1.024
25	1.000	.000	.000	.000	.000	.000	.000	.000	.000	.000	.000	.000
26	1.088	1.088	1.141	1.162	.788	.915	.923	1.074	1.131	1.060	.713	.903
27	.000	.000	.000	.000	.000	.000	.000	.000	.000	.000	.000	.000
				SHARP	LEADING	EDGE	WITH	TRIPS				
30	1.075	.870	.906	1.014	.718	.722	.814	.866	.980	1.010	.531	.721
31	1.047	.892	.935	1.005	.757	.825	.869	.924	.967	.988	.685	.838
32	.991	.959	.939	.972	.883	.694	.877	.901	.923	.952	.836	.873

Table V. Continued

Run	$\frac{q_{37}}{q_{fp}}$	$\frac{q_{38}}{q_{fp}}$	$\frac{q_{39}}{q_{fp}}$	$\frac{q_{40}}{q_{fp}}$	$\frac{q_{41}}{q_{fp}}$	$\frac{q_{42}}{q_{fp}}$	$\frac{q_{43}}{q_{fp}}$	$\frac{q_{44}}{q_{fp}}$	$\frac{q_{45}}{q_{fp}}$	$\frac{q_{46}}{q_{fp}}$	$\frac{q_{47}}{q_{fp}}$	$\frac{q_{48}}{q_{fp}}$
							BLUNT LEADING EDGE WITHOUT TRIPS					
6	1.476	.658	1.088	1.285	1.387	1.454	1.524	1.370	1.401	1.728	1.764	1.692
7	1.320	.401	.746	1.122	1.276	1.300	1.318	.795	.982	1.219	1.344	1.437
8	1.434	.717	1.077	1.106	1.158	1.186	1.149	.776	1.087	1.130	1.128	1.164
9	1.199	.722	.950	1.044	1.131	1.170	1.215	.977	1.076	1.118	1.196	1.266
10	1.407	.424	1.027	1.203	1.359	1.361	1.459	.768	1.398	1.619	1.657	1.607
11	1.226	.872	1.112	1.147	1.164	1.205	1.212	.890	1.128	1.252	1.275	1.298
12	1.237	1.047	1.081	1.103	1.170	1.189	1.229	.976	1.069	1.160	1.218	1.259
13	.000	.000	.000	.000	.000	.000	.000	.000	.000	.000	.000	.000
14	1.563	.763	1.224	1.355	1.398	1.501	1.559	2.098	2.150	1.985	1.781	1.743
15	.000	.000	.000	.000	.000	.000	.000	.000	.000	.000	.000	.000
							BLUNT LEADING EDGE WITH TRIPS					
19	.860	.500	.670	.736	.804	.863	.909	1.100	.935	.934	.944	.965
20	.938	.733	.849	.868	.911	.946	.952	1.000	1.033	1.031	1.018	1.010
21	1.006	.789	.892	.912	.946	.964	1.016	1.057	1.040	1.024	1.050	1.061
22	1.092	.698	.755	.841	.990	1.056	1.110	1.279	1.165	1.203	1.194	1.177
23	1.072	.807	.912	.952	.985	1.000	1.038	1.171	1.136	1.107	1.088	1.056
24	1.034	.930	.940	.955	.984	.999	.999	1.173	1.120	1.114	1.066	1.055
25	.000	.000	.000	.000	.000	.000	.000	.000	.000	.000	.000	.000
26	1.069	.560	.729	.824	.932	1.008	1.022	1.252	1.243	1.208	1.157	1.087
27	.000	.000	.000	.000	.000	.000	.000	.000	.000	.000	.000	.000
							SHARP LEADING EDGE WITH TRIPS					
30	.947	.529	.544	.630	.827	.934	1.002	1.134	.998	1.054	1.075	1.106
31	.952	.639	.753	.837	.907	.000	1.001	.969	1.068	.999	1.012	-.003
32	.933	.812	.832	.862	.898	.910	.932	1.000	.996	.997	.997	1.011

23

Table V. Concluded

Run	$\dfrac{q_{49}}{q_{fp}}$	$\dfrac{q_{50}}{q_{fp}}$	$\dfrac{q_{51}}{q_{fp}}$	$\dfrac{q_{52}}{q_{fp}}$	$\dfrac{q_{53}}{q_{fp}}$	$\dfrac{q_{54}}{q_{fp}}$	$\dfrac{q_{55}}{q_{fp}}$	$\dfrac{q_{56}}{q_{fp}}$	$\dfrac{q_{57}}{q_{fp}}$	$\dfrac{q_{58}}{q_{fp}}$
					BLUNT LEADING EDGE WITHOUT TRIPS					
6	1.674	1.110	1.917	1.776	.788	1.896	1.811	.769	1.902	1.857
7	1.429	.629	1.433	1.498	.567	1.440	1.508	.639	1.427	1.492
8	1.179	.313	1.118	1.224	.388	1.118	1.203	.710	1.141	1.164
9	1.236	.937	1.117	1.254	.934	1.166	1.218	.748	1.075	1.100
10	1.572	.840	1.818	1.683	.732	1.802	1.741	.750	1.804	1.777
11	1.300	1.062	1.316	1.264	1.075	1.337	1.314	1.086	1.331	1.309
12	1.314	1.151	1.232	1.305	1.046	1.178	1.305	1.115	1.122	1.303
13	.000	.000	.000	.000	.000	.000	.000	.000	.000	.000
14	1.572	1.896	2.113	1.853	1.624	2.160	1.789	1.317	2.097	1.821
15	.000	.000	.000	.000	.000	.000	.000	.000	.000	.000
					BLUNT LEADING EDGE WITH TRIPS					
19	.943	.860	1.098	1.026	.835	1.199	1.075	.945	1.239	1.089
20	1.011	.789	1.068	1.070	.859	1.082	1.070	1.010	1.113	1.060
21	1.062	1.003	1.074	1.112	.986	1.116	1.137	.893	1.132	1.121
22	1.207	1.331	1.396	1.264	1.208	1.501	1.295	1.128	1.558	1.335
23	1.044	1.221	1.149	1.054	1.185	1.151	1.077	1.139	1.150	1.093
24	1.060	1.201	1.134	1.078	1.070	1.099	1.110	1.022	1.077	1.135
25	.000	.000	.000	.000	.000	.000	.000	.000	.000	.000
26	.949	1.483	1.301	1.122	1.507	1.341	1.090	1.104	1.315	1.077
27	.000	.000	.000	.000	.000	.000	.000	.000	.000	.000
					SHARP LEADING EDGE WITH TRIPS					
30	1.427	1.322	1.346	1.197	1.443	1.617	1.281	1.521	1.754	1.359
31	1.035	1.108	1.082	1.042	1.262	1.152	1.093	1.339	1.221	1.126
32	1.024	1.082	1.075	1.062	1.074	1.176	1.115	1.149	1.214	1.176

24

Figure 1. Dome model installed in panel holder of the Langley 8-Foot High-Temperature Tunnel.

L-84-2520

25
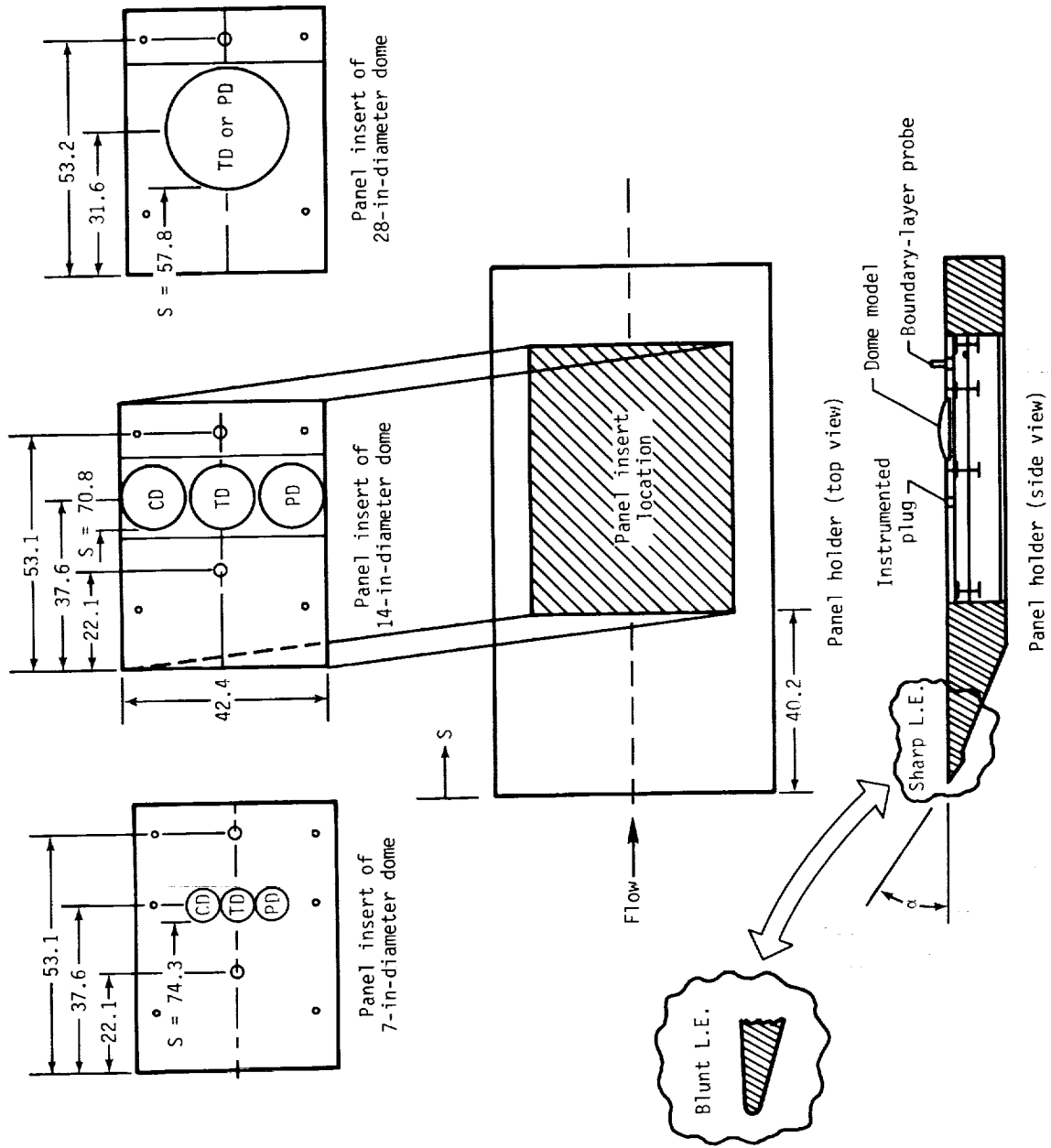
Figure 2. Schematic diagram of panel holder with panel inserts of dome model. All dimensions are given in inches.
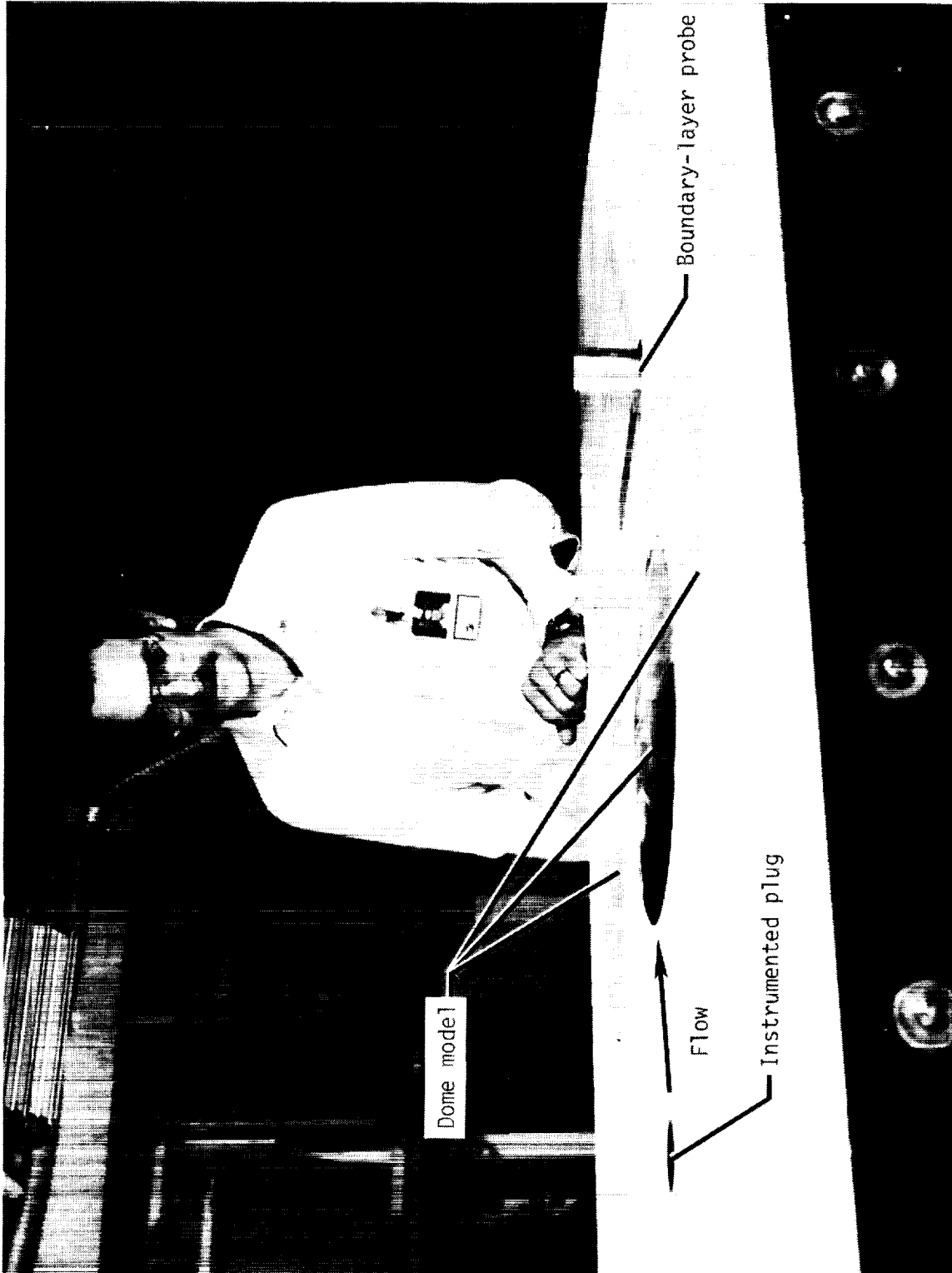
Figure 3. Normal locations of instrumented plug and boundary-layer probe.

L-84-2522

27
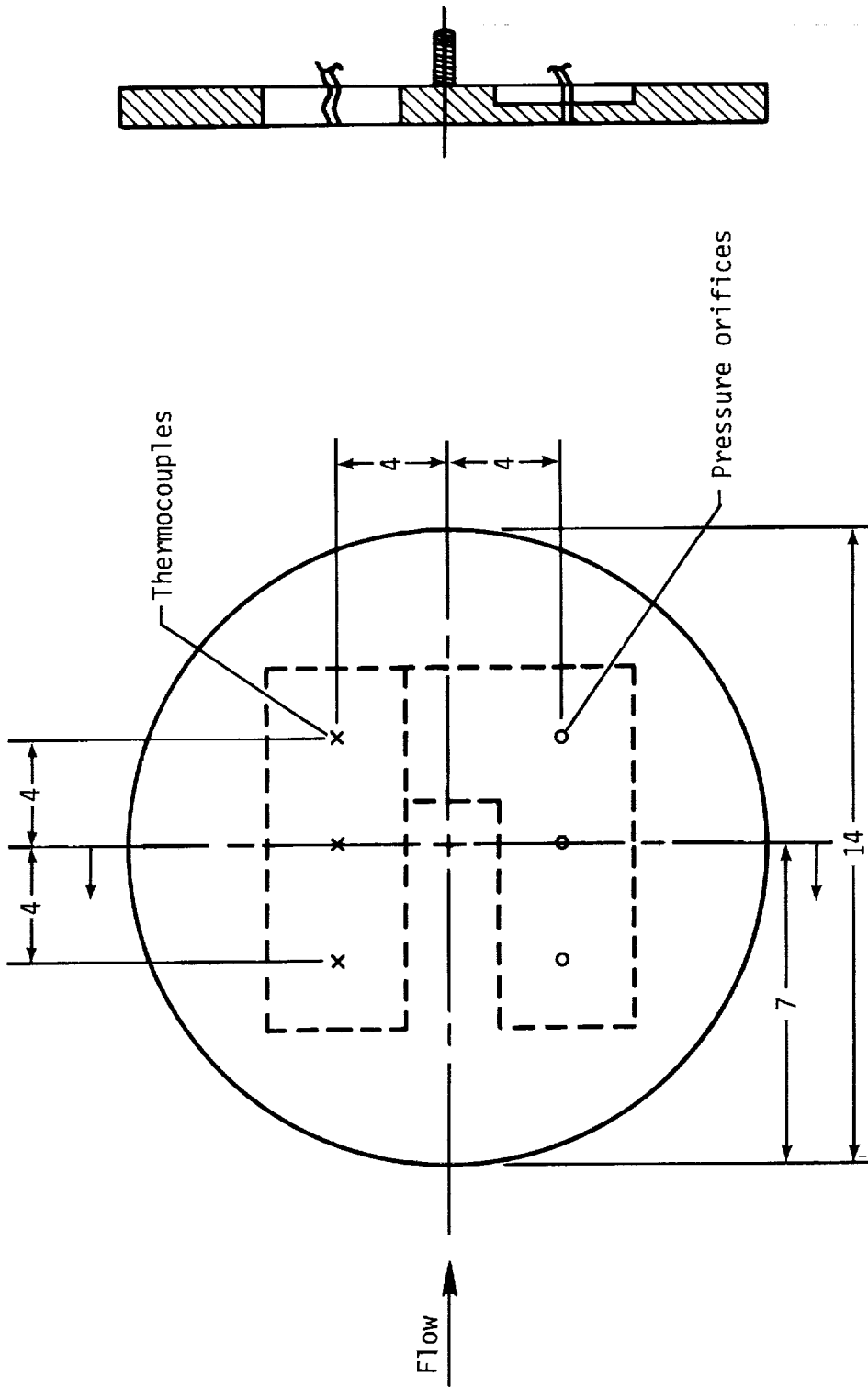
Figure 4. Flat calibration disk. All dimensions are given in inches.
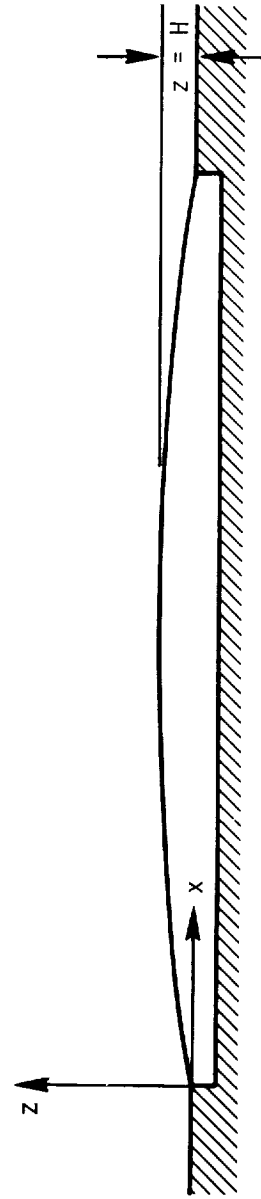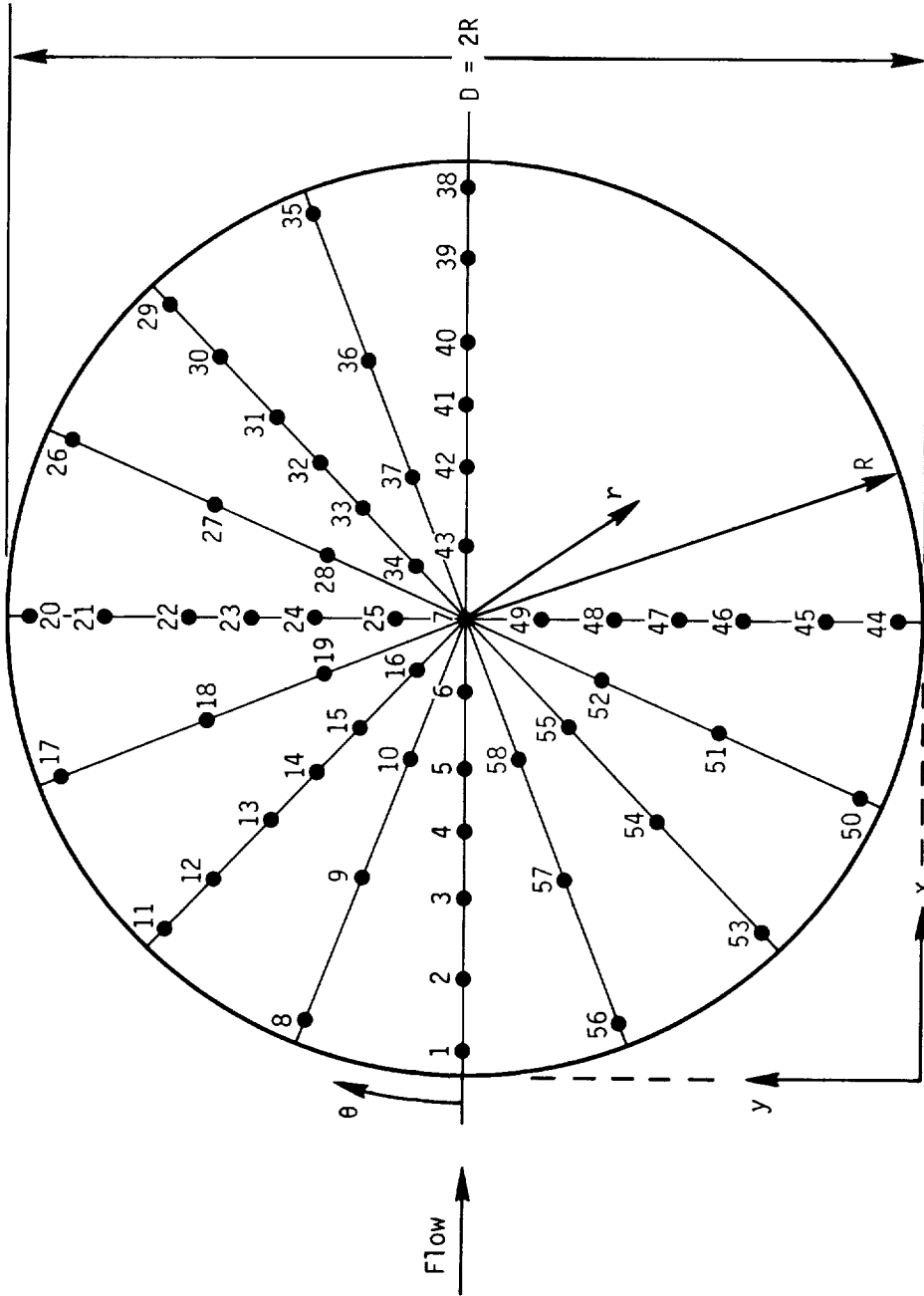
Figure 5. Instrumented locations for both pressure- and thermocouple-instrumented domes.

(a) Instrumented plug.

Probe	z, in.
1	0.032
2	.096
3	.160
4	.224
5	.288
6	.416
7	.544
8	.673
9	.800
10	.928
11	1.12
12	1.44
13	2.00
14	2.50
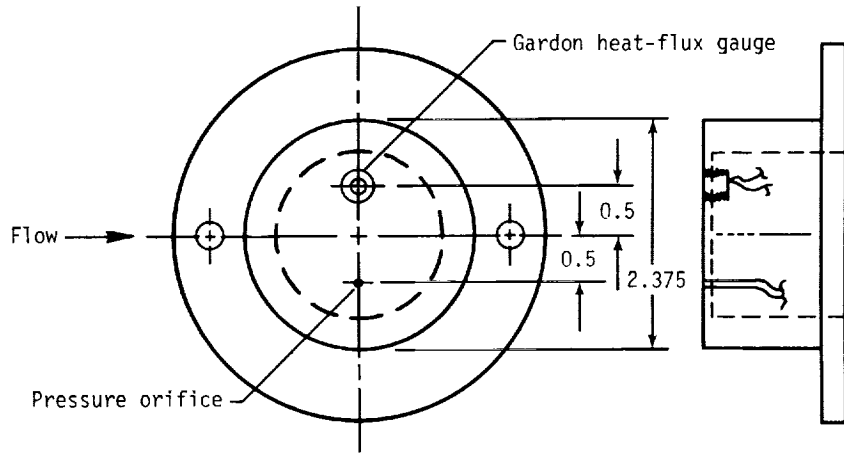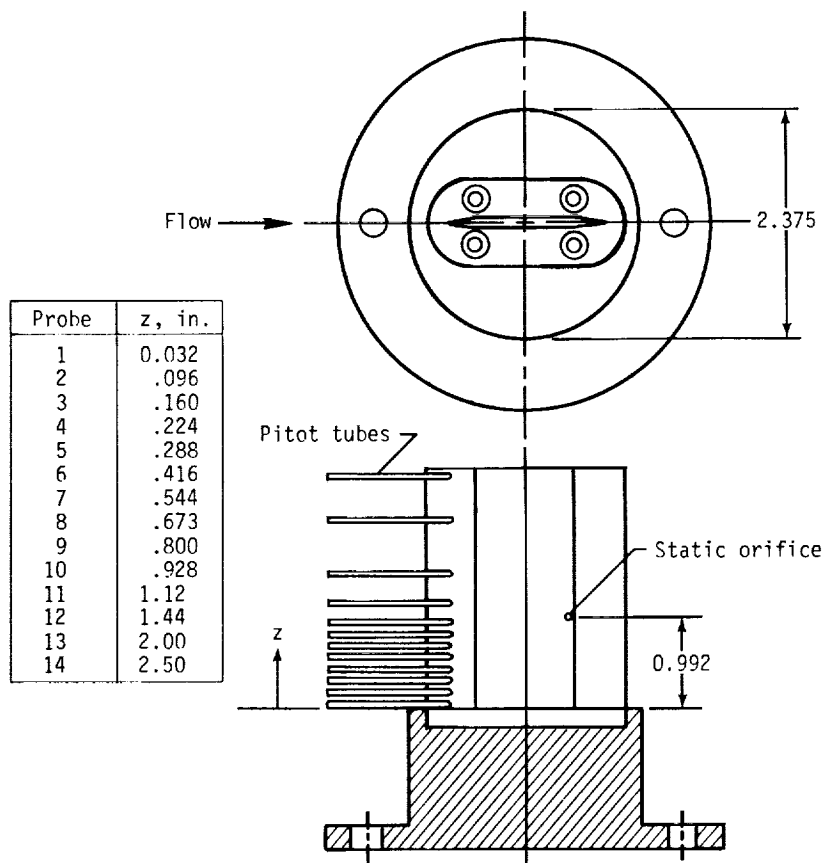
(b) Boundary-layer probe.

Figure 6. Additional panel holder instrumentation. All dimensions are given in inches.

Fuel

Air

Combustor

Test chamber

Nozzle

Pod

Supersonic diffuser

Mixing tube

Air ejector

Diffuser
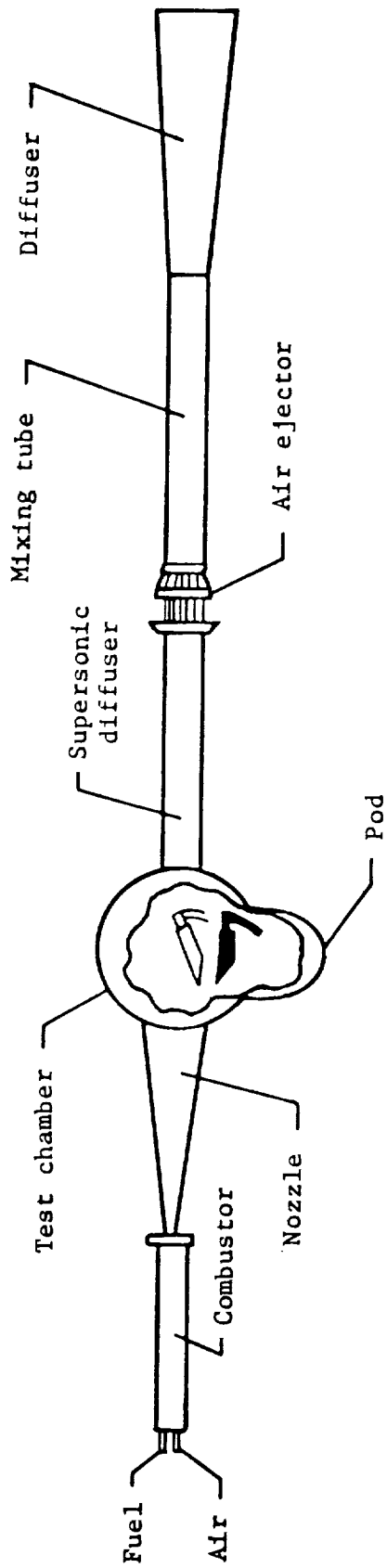
Figure 7. The Langley 8-Foot High-Temperature Tunnel.

31

○   Experimental data

— — — —   B.L. solution (ref. 16)
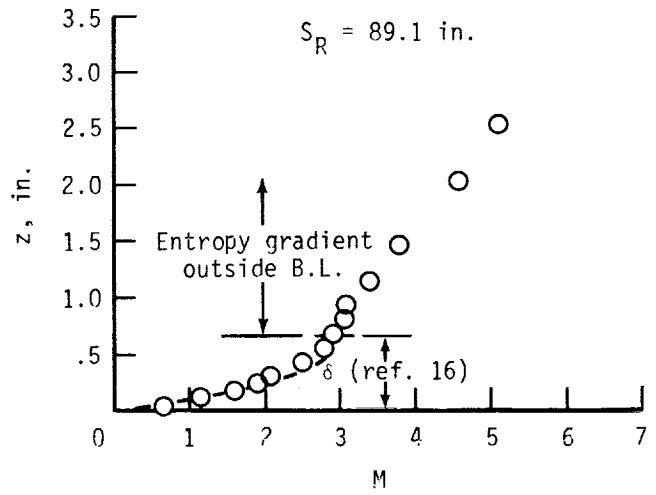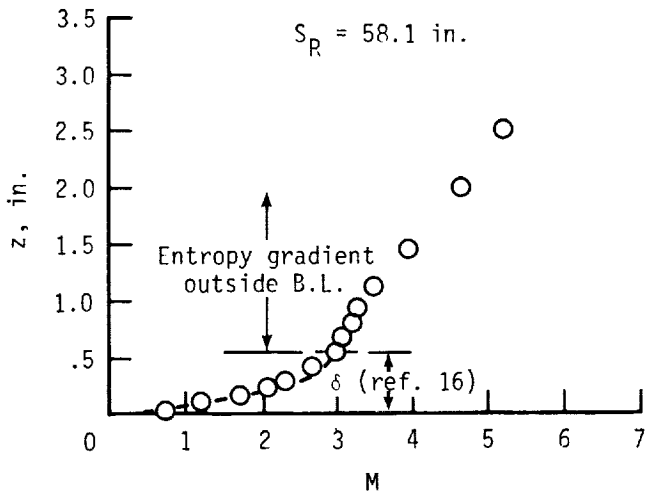
(a) Laminar boundary layer (no trips). Case 1.
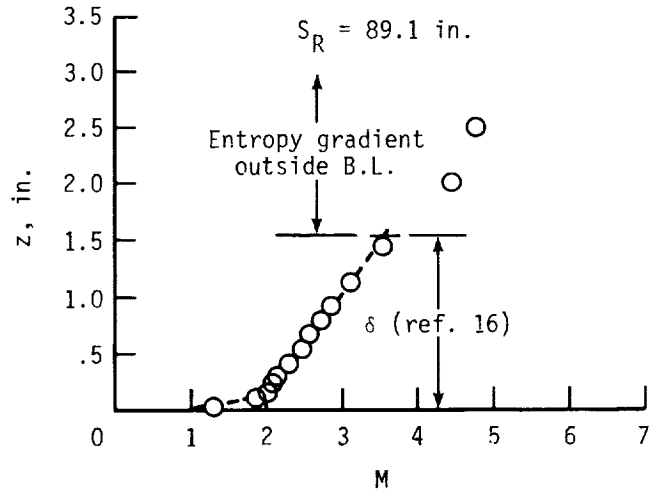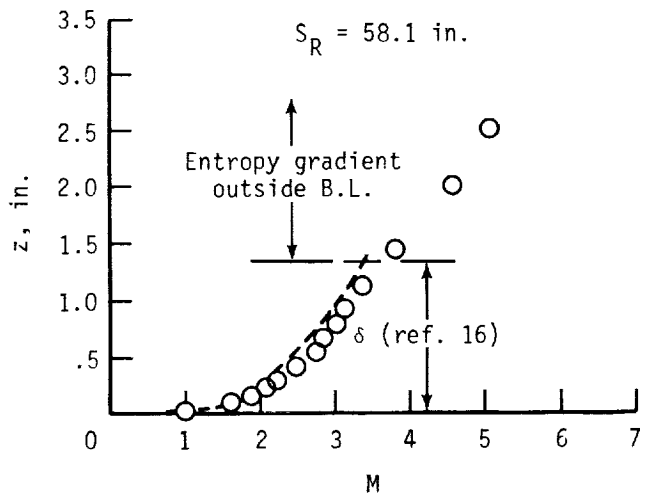
(b) Turbulent boundary layer (with trips). Case 2.

Figure 8. Mach number profiles for undisturbed flow with blunt leading edge.
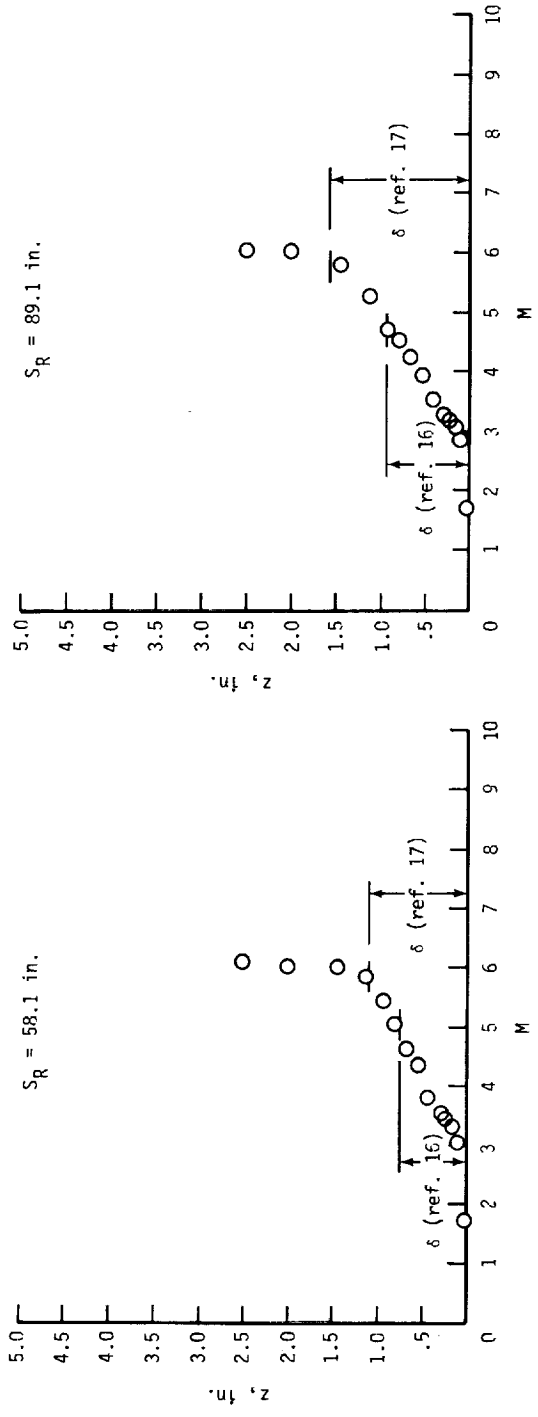
(a) Mach number profiles.
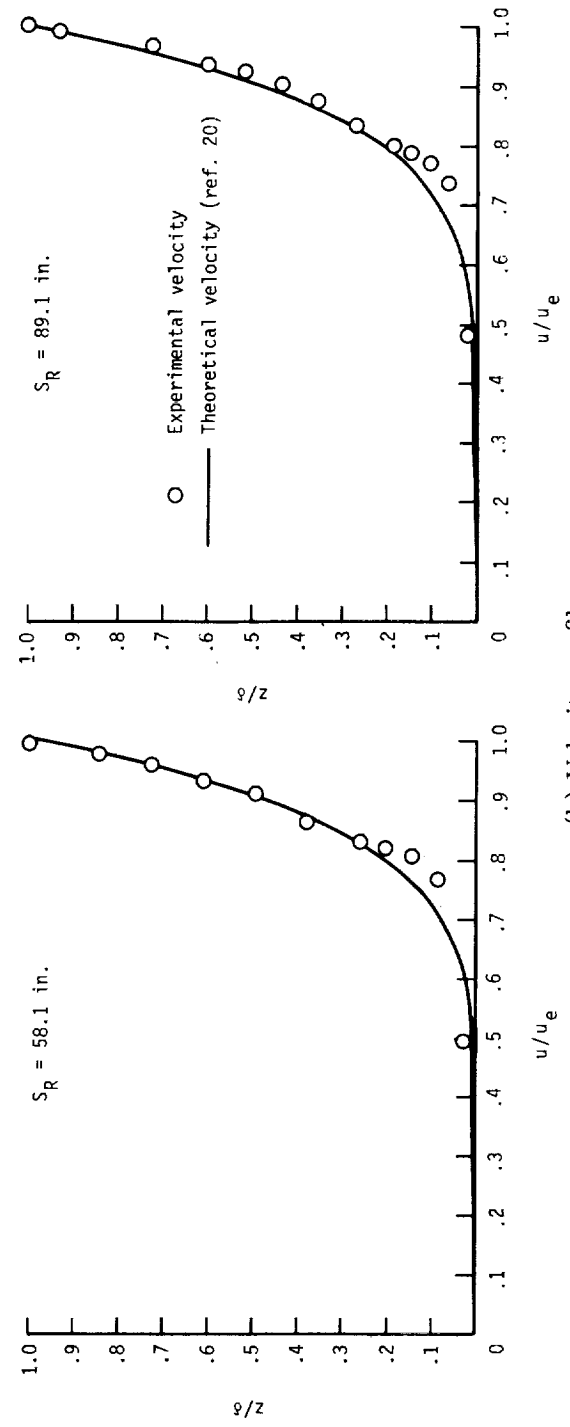
(b) Velocity profiles.

Figure 9. Boundary-layer profiles for undisturbed flow with sharp leading edge.
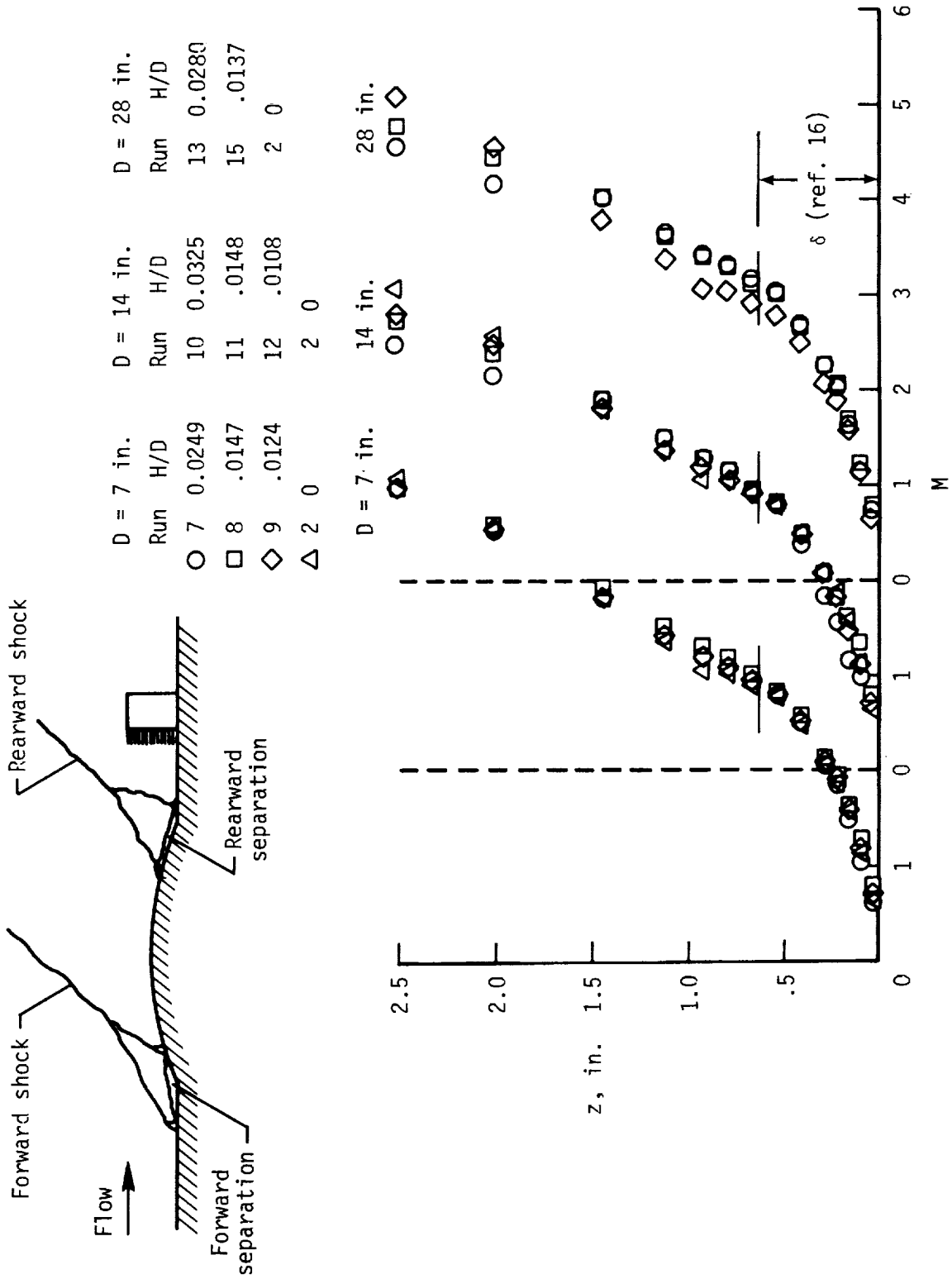
Figure 10. Wake disturbance behind protuberance for laminar boundary layer with blunt leading edge (no trips). Case 1.
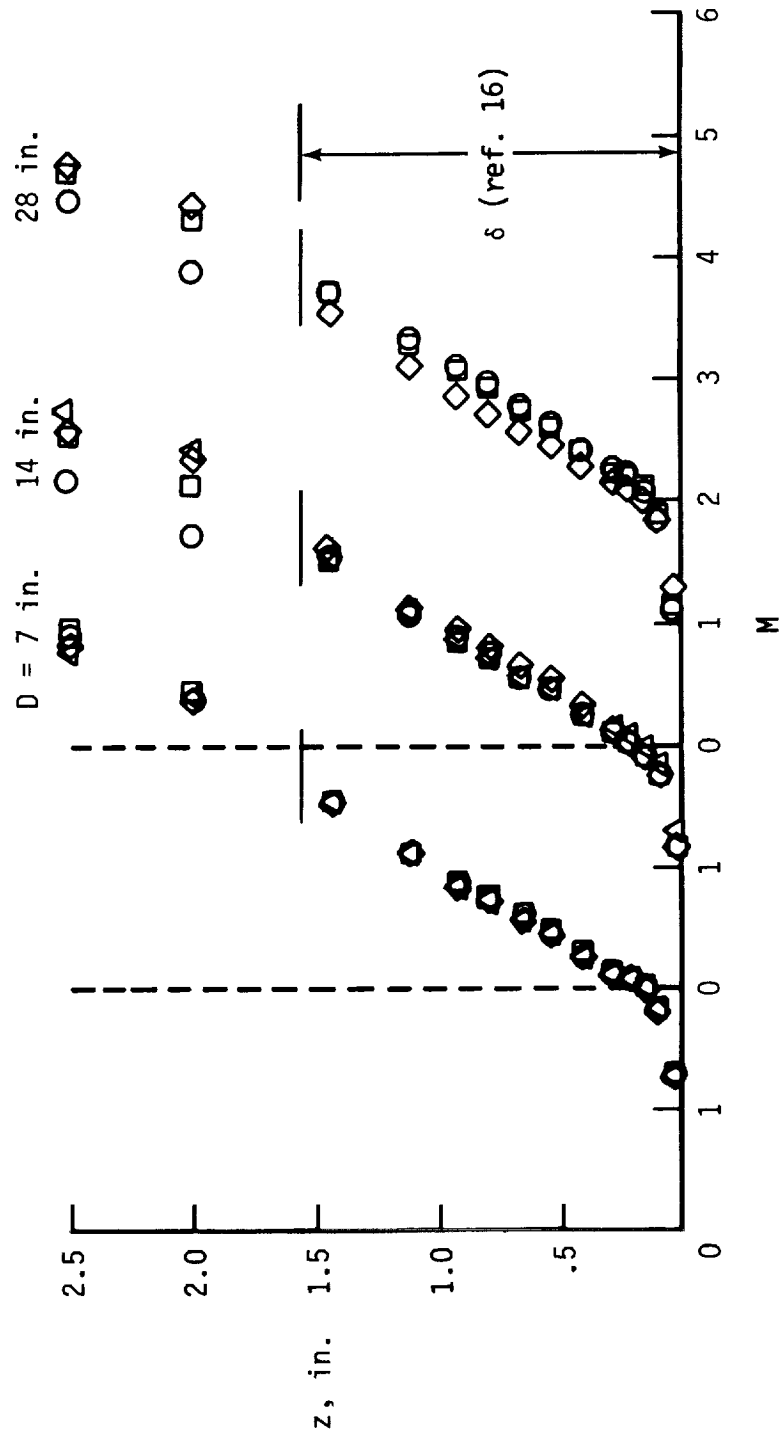
Figure 11. Wake disturbance behind protuberance for turbulent boundary layer with blunt leading edge (with trips). Case 2.
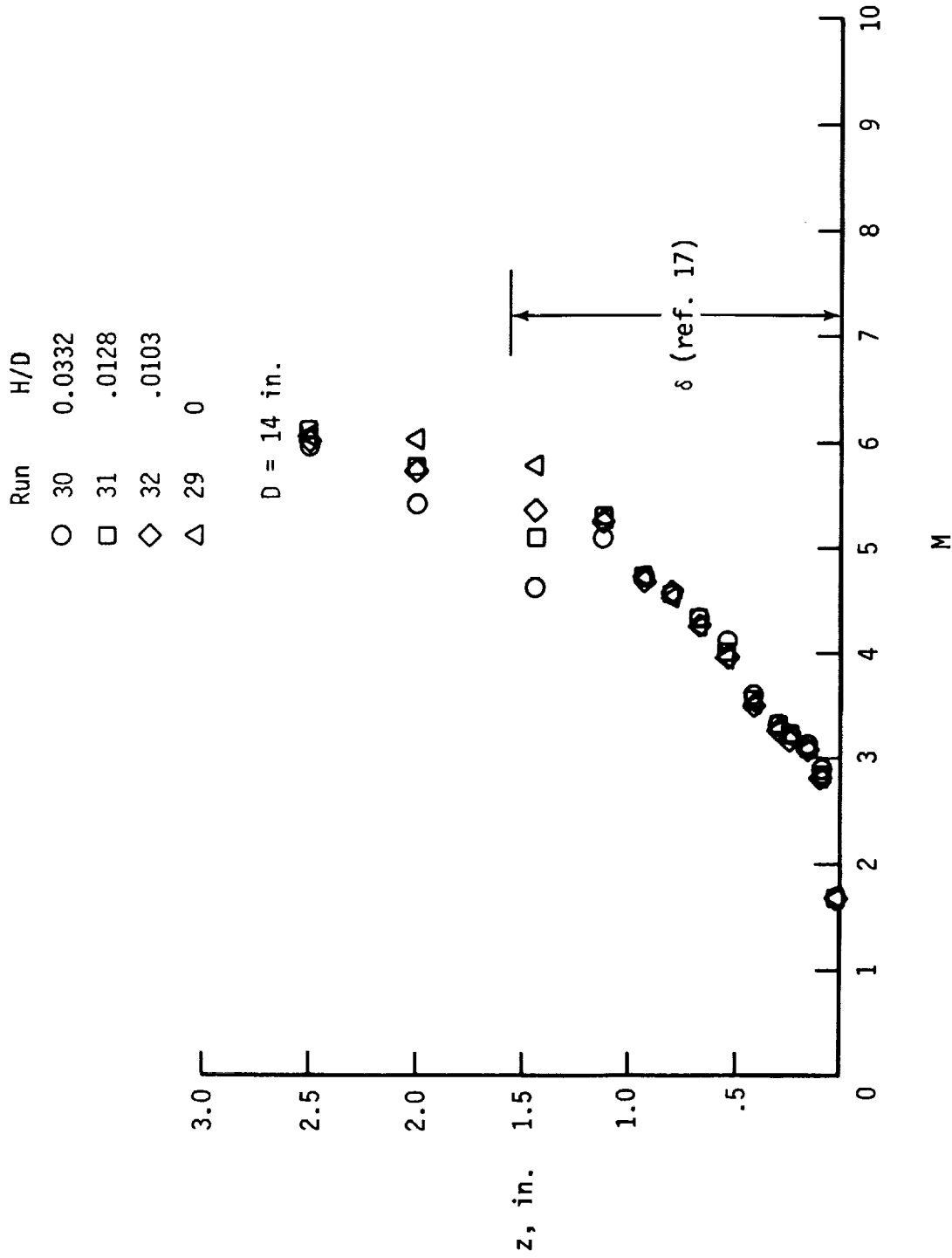
Figure 12. Wake disturbance behind protuberance for turbulent boundary layer with sharp leading edge (with trips). Case 3.
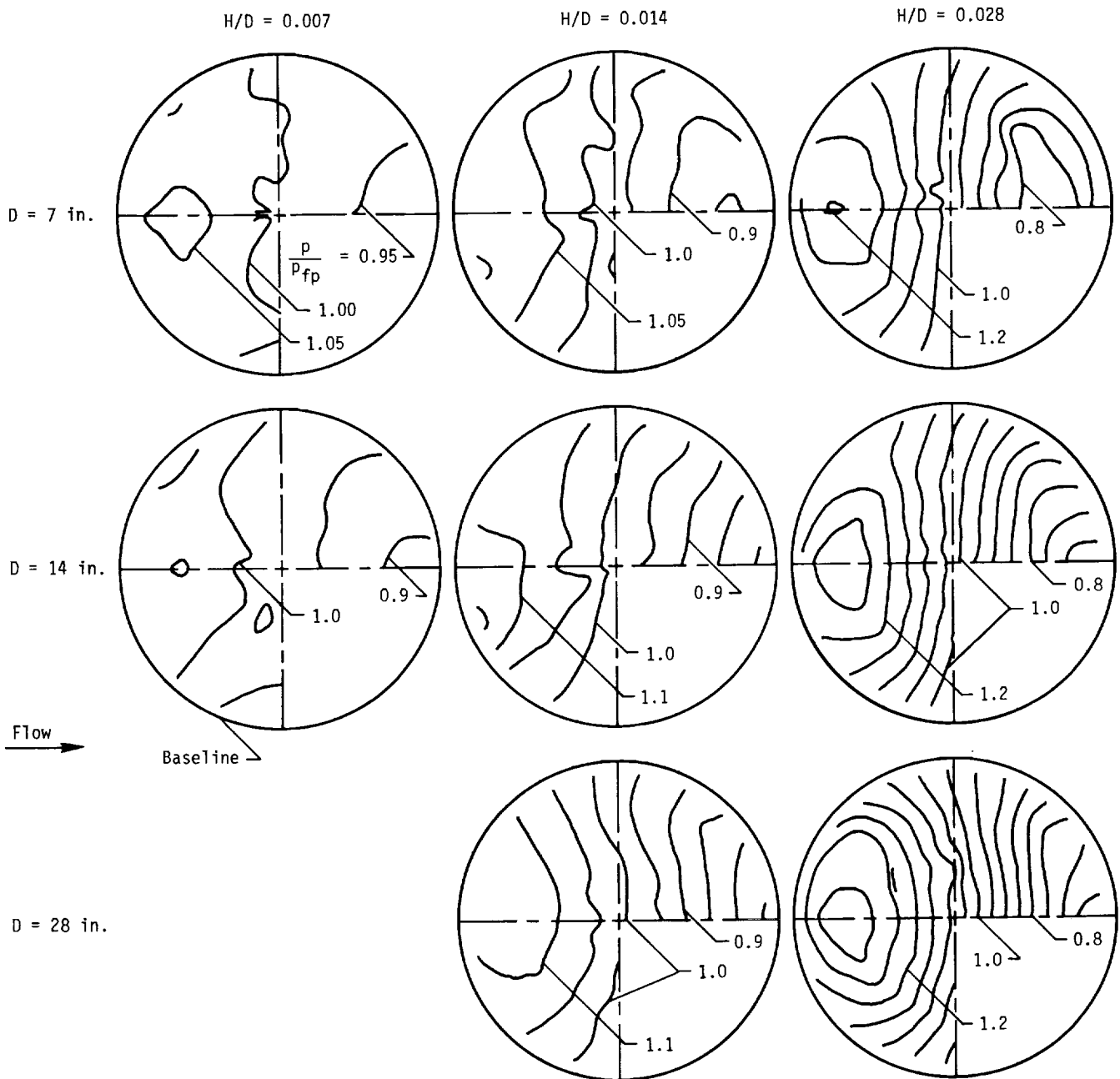
(a) Laminar boundary layer with blunt leading edge (no trips). Case 1.

Figure 13. Overview of normalized pressure contour. Nominal H/D conditions.

H/D = 0.007   H/D = 0.014   H/D = 0.028

D = 7 in.

$$\frac{p}{p_{fp}} = 0.95$$
1.00
1.05

0.9
1.0
1.1

0.8
1.0
1.2

D = 14 in.

0.95
1.00
1.05

0.9
1.0
1.1

0.8
1.0
1.2

Flow

Baseline

D = 28 in.

1.0
0.9
1.1

1.0
0.8
1.2
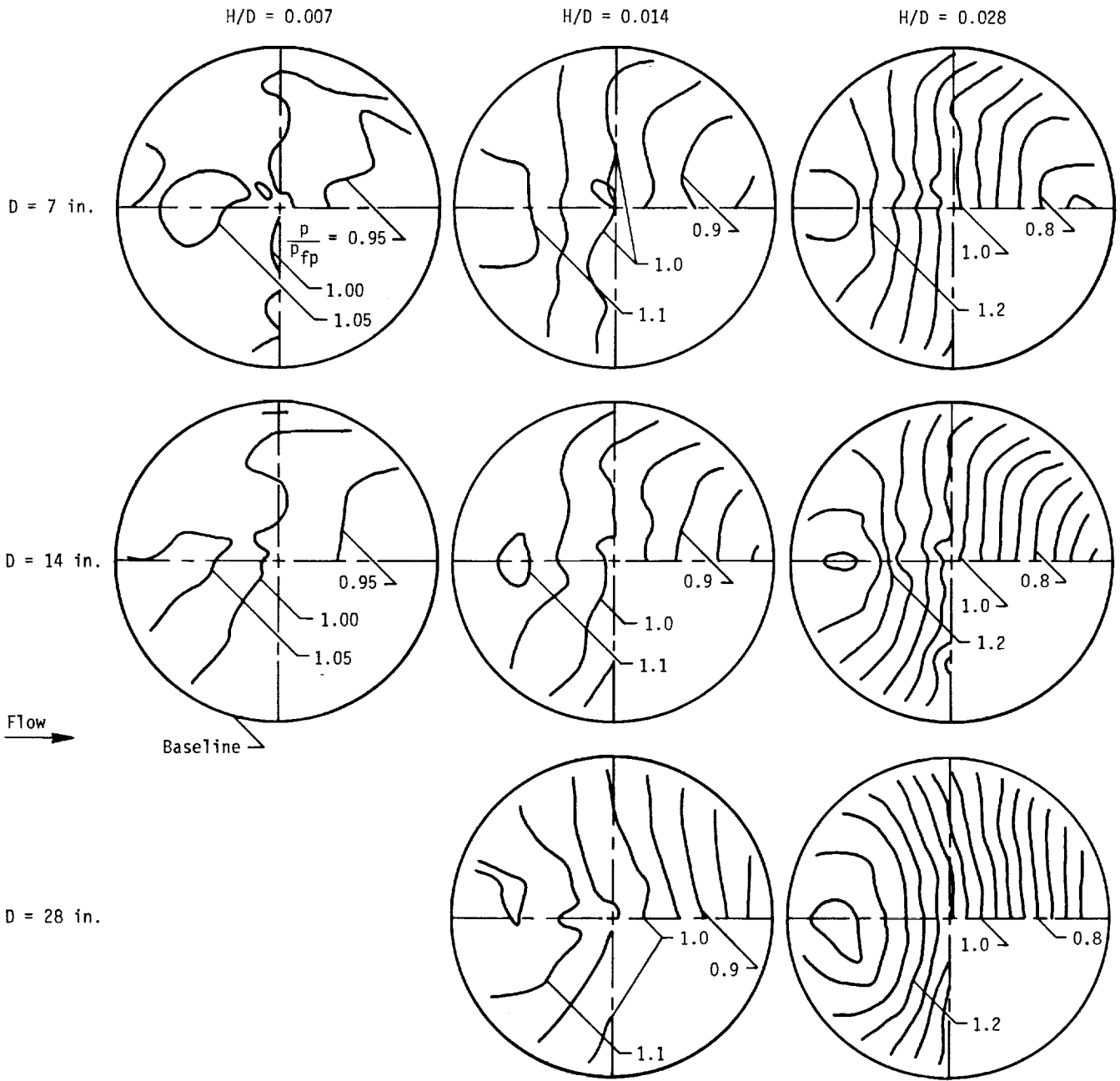
(b) Turbulent boundary layer with blunt leading edge (with trips). Case 2.

Figure 13. Continued.

38

H/D = 0.007   H/D = 0.014   H/D = 0.028

Flow

D = 14 in.

$\frac{p}{p_{fp}} = 0.9$

1.0

1.1

0.8

1.0

1.2

0.6

1.0

1.4

Baseline
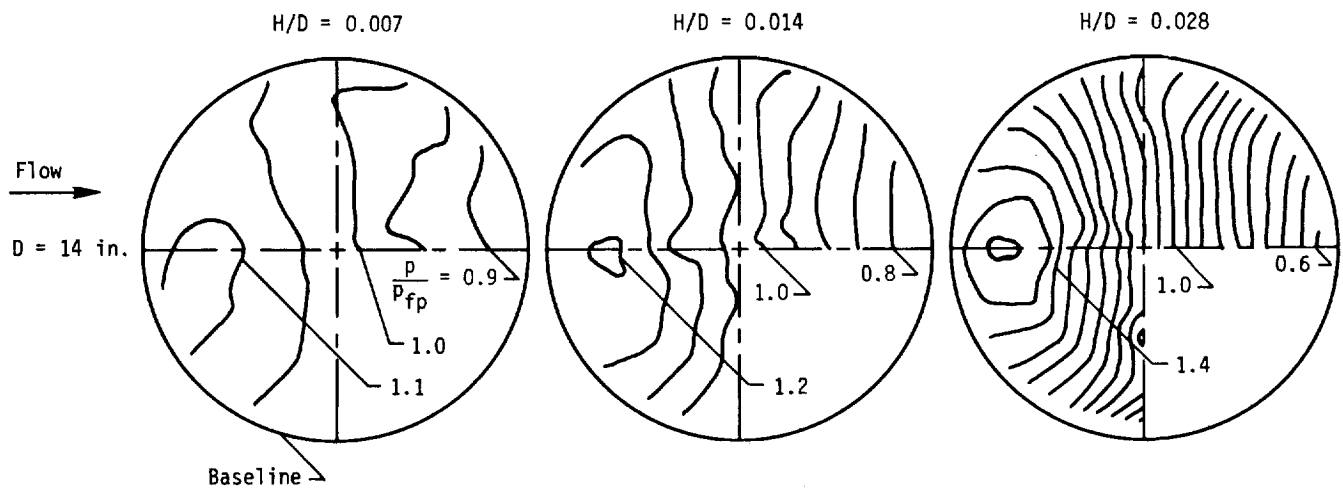
(c) Turbulent boundary layer with sharp leading edge (with trips). Case 3.

Figure 13. Concluded.
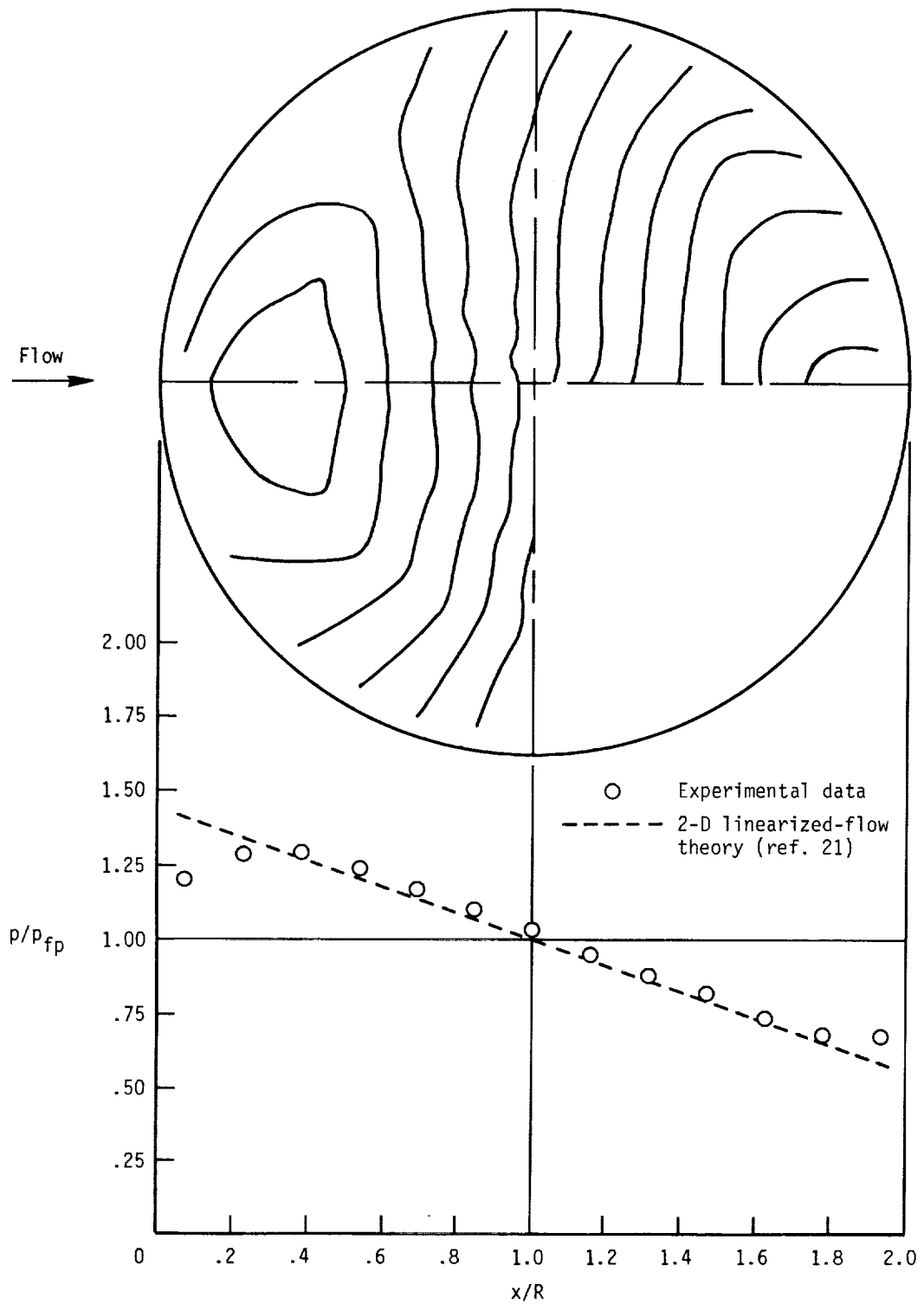
(a) Laminar boundary layer with blunt leading edge (no trips). Case 1.

Figure 14. Contour and longitudinal pressure distributions. $D = 14$ in.; $H = 0.4$ in.
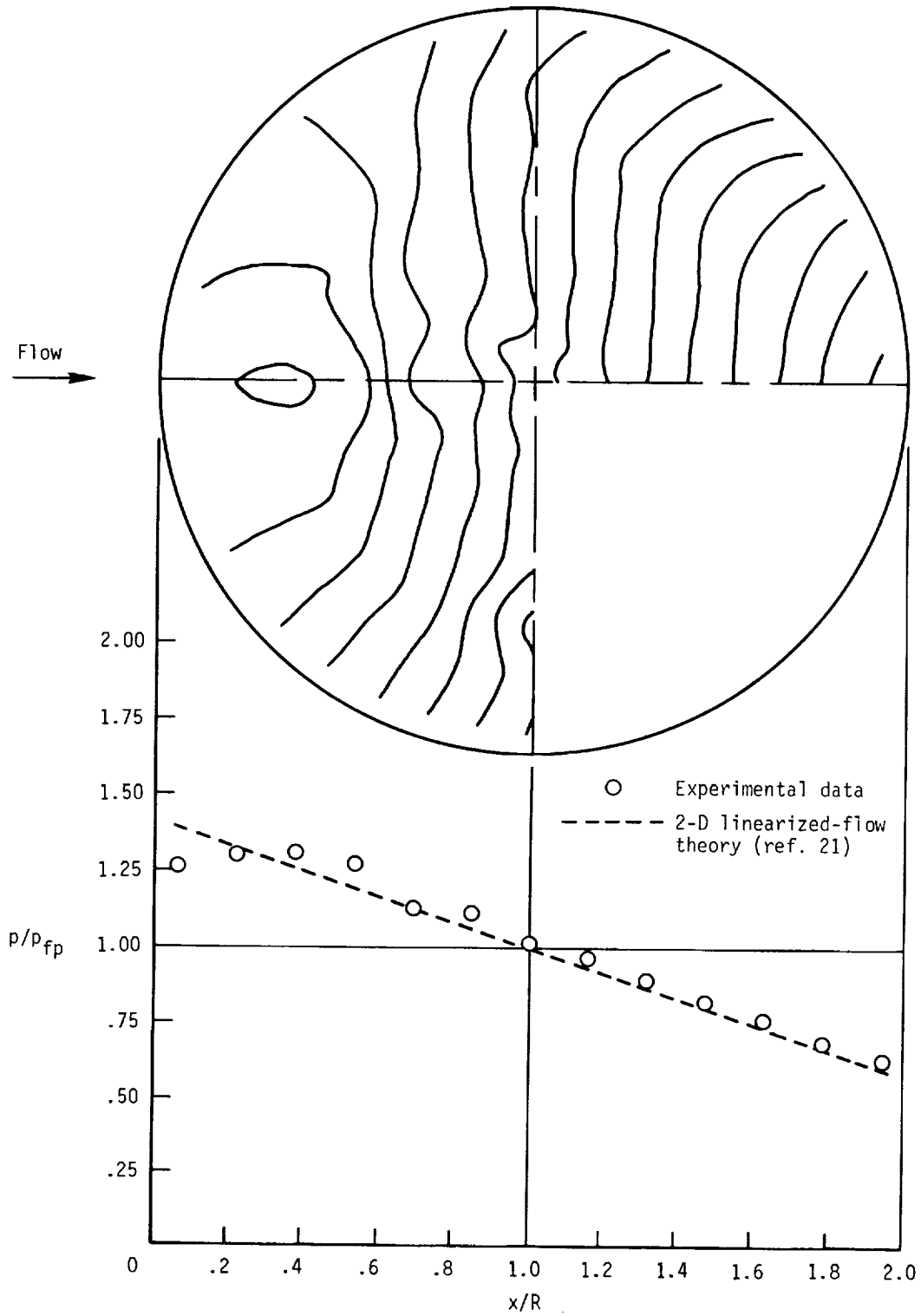
(b) Turbulent boundary layer with blunt leading edge (with trips). Case 2.

Figure 14. Continued.
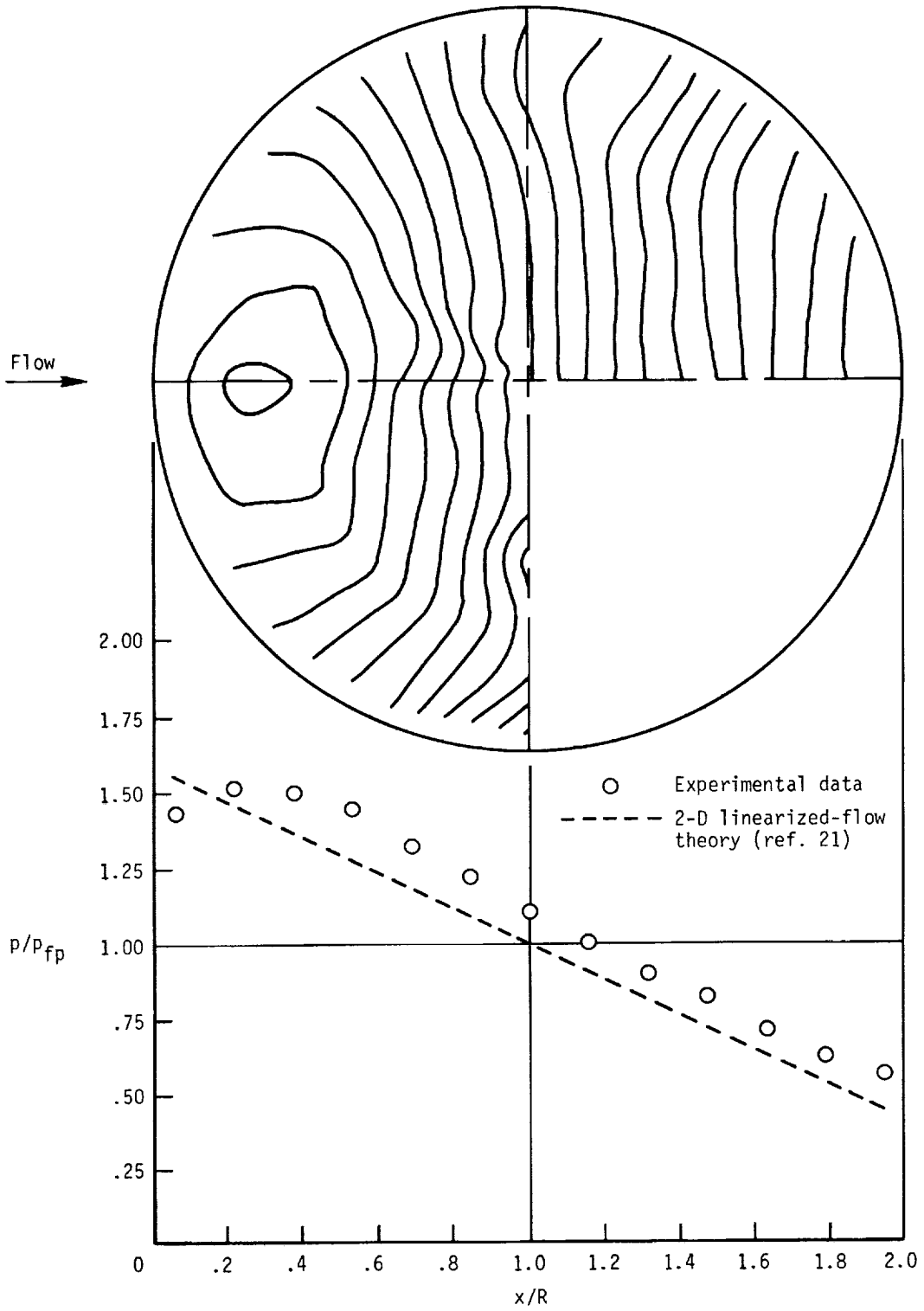
(c) Turbulent boundary layer with sharp leading edge (with trips). Case 3.

Figure 14. Concluded.
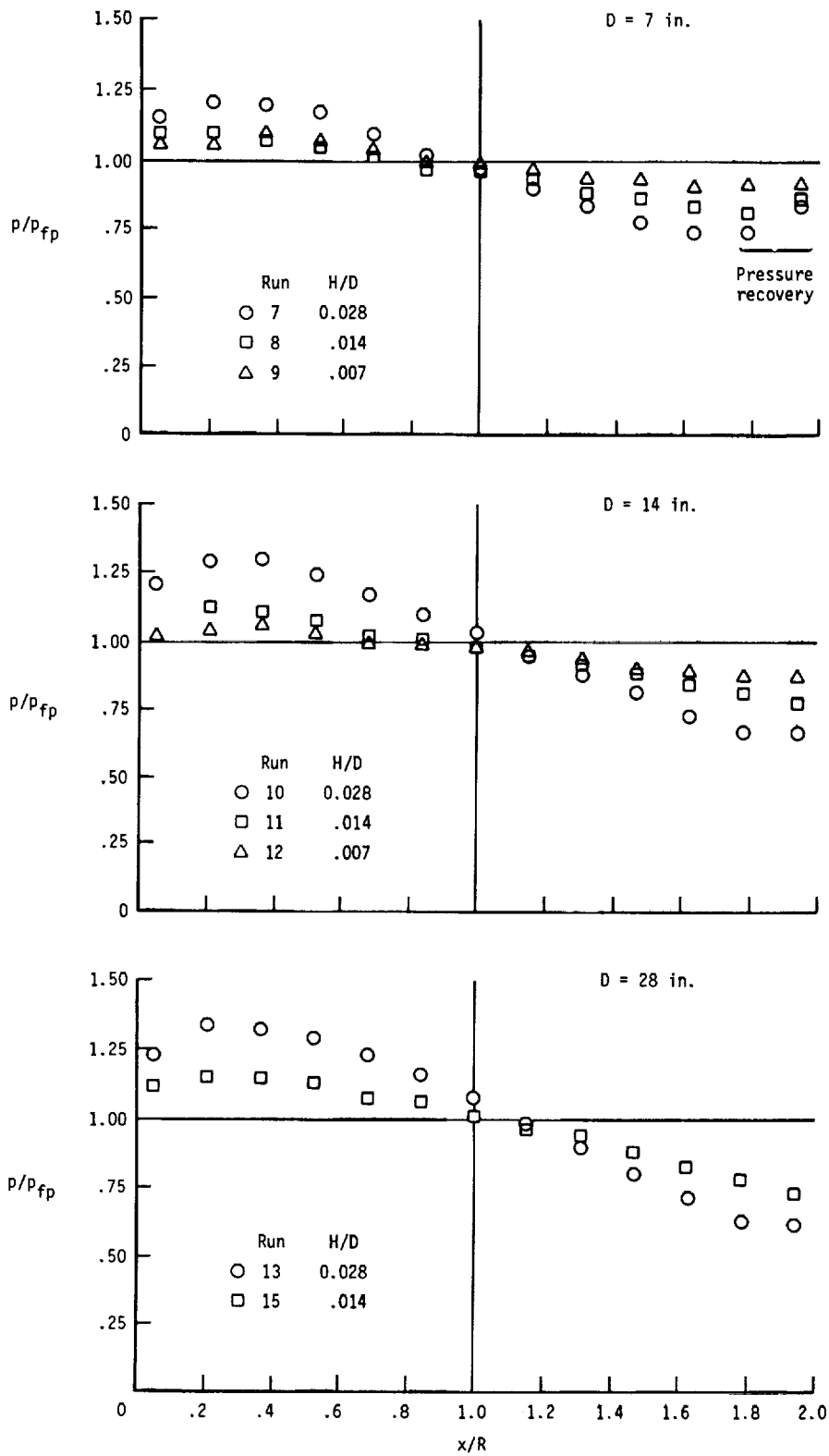
(a) Laminar boundary layer with blunt leading edge (no trips). Case 1; run 12 is baseline condition.

Figure 15. Longitudinal pressure distributions on protuberances.
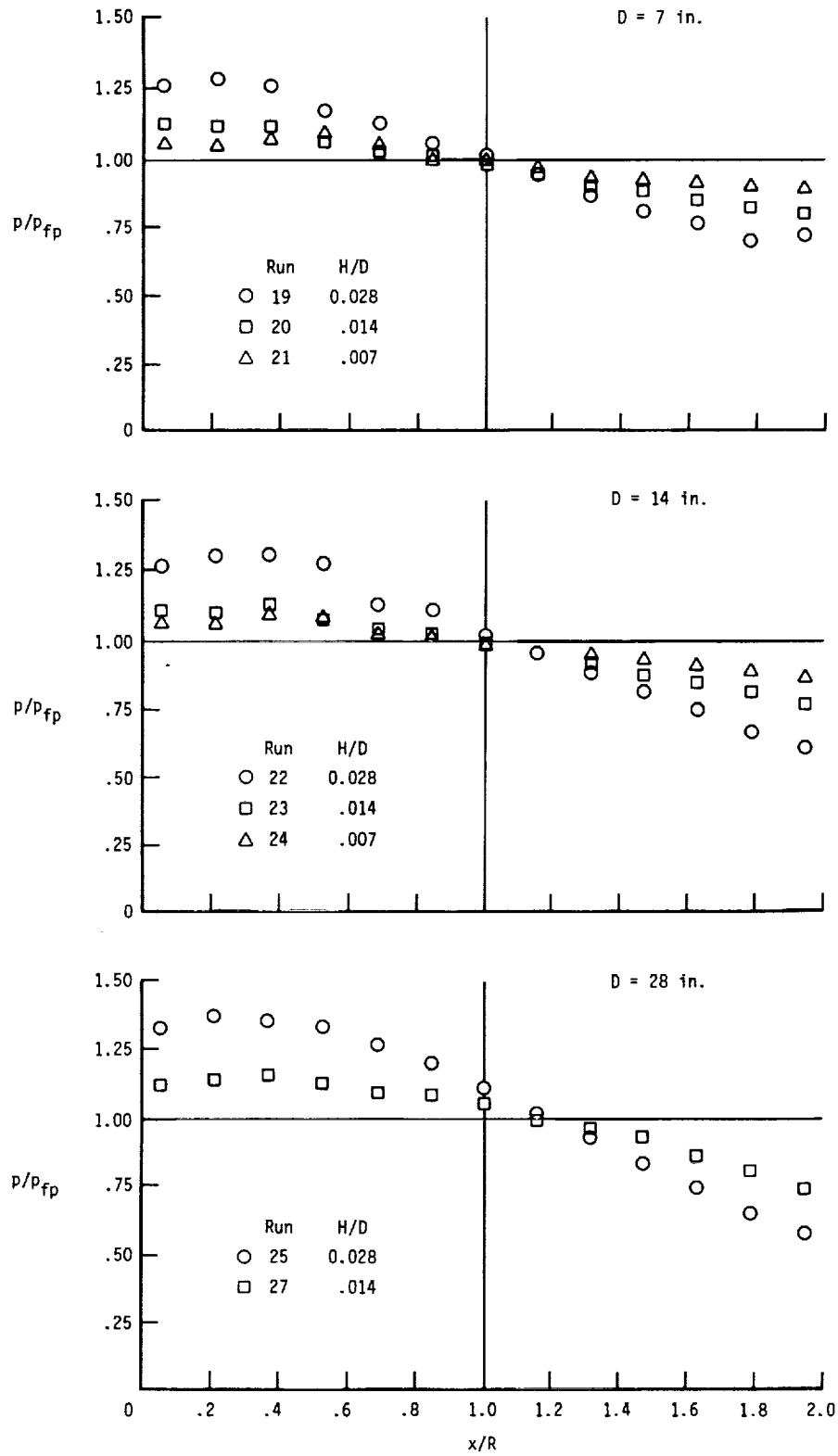
(b) Turbulent boundary layer with blunt leading edge (with trips). Case 2; run 24 is baseline condition.

Figure 15. Continued.
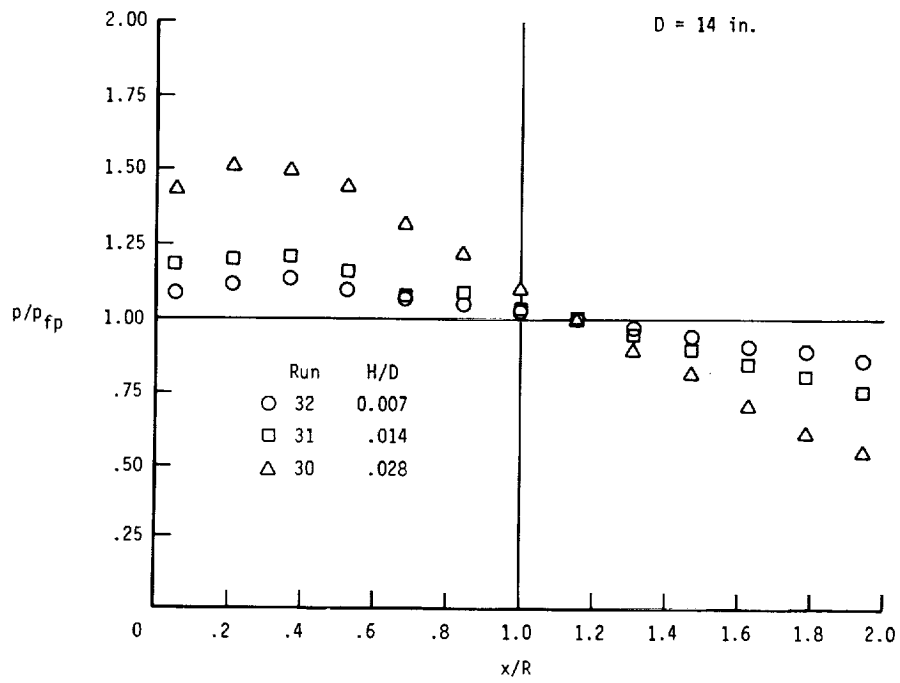
(c) Turbulent boundary layer with sharp leading edge (with trips). Case 3; run 32 is baseline condition.

Figure 15. Concluded.
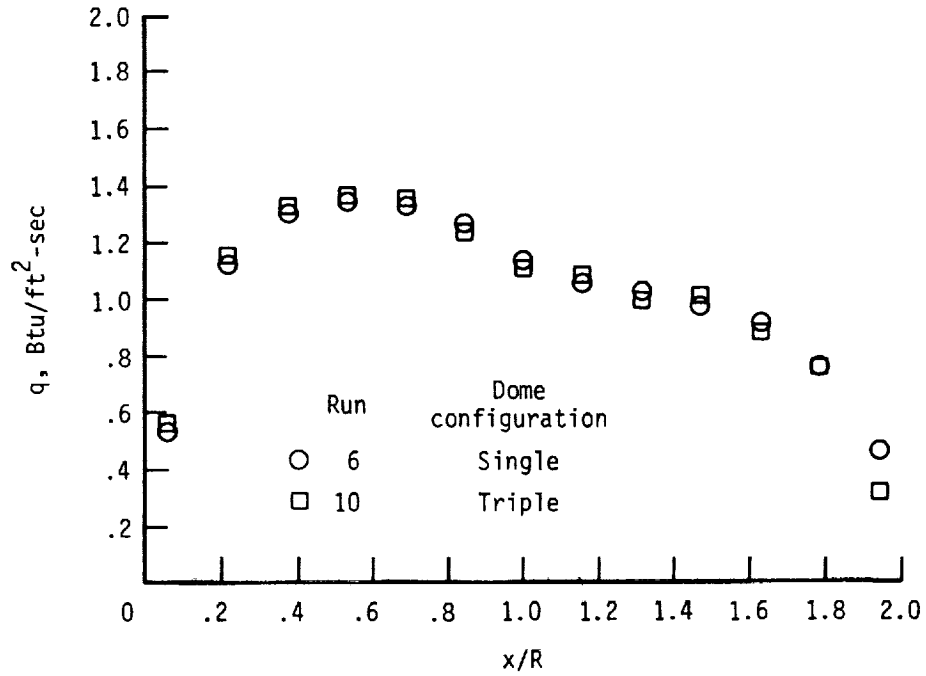
(a) Longitudinal heating-rate distribution.
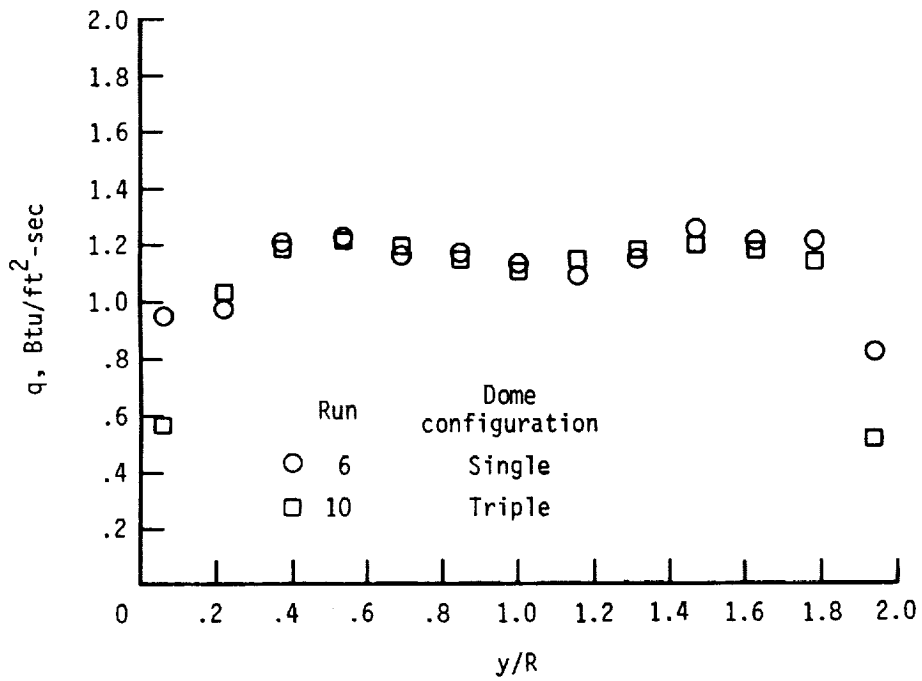
(b) Lateral heating-rate distribution.

Figure 16. Longitudinal and lateral heating-rate distributions with and without adjacent dome.

H/D = 0.007   H/D = 0.014   H/D = 0.028

D = 7 in.

$$\frac{q}{q_{fp}} = 1.2$$

D = 14 in.

Flow

Baseline

D = 28 in.
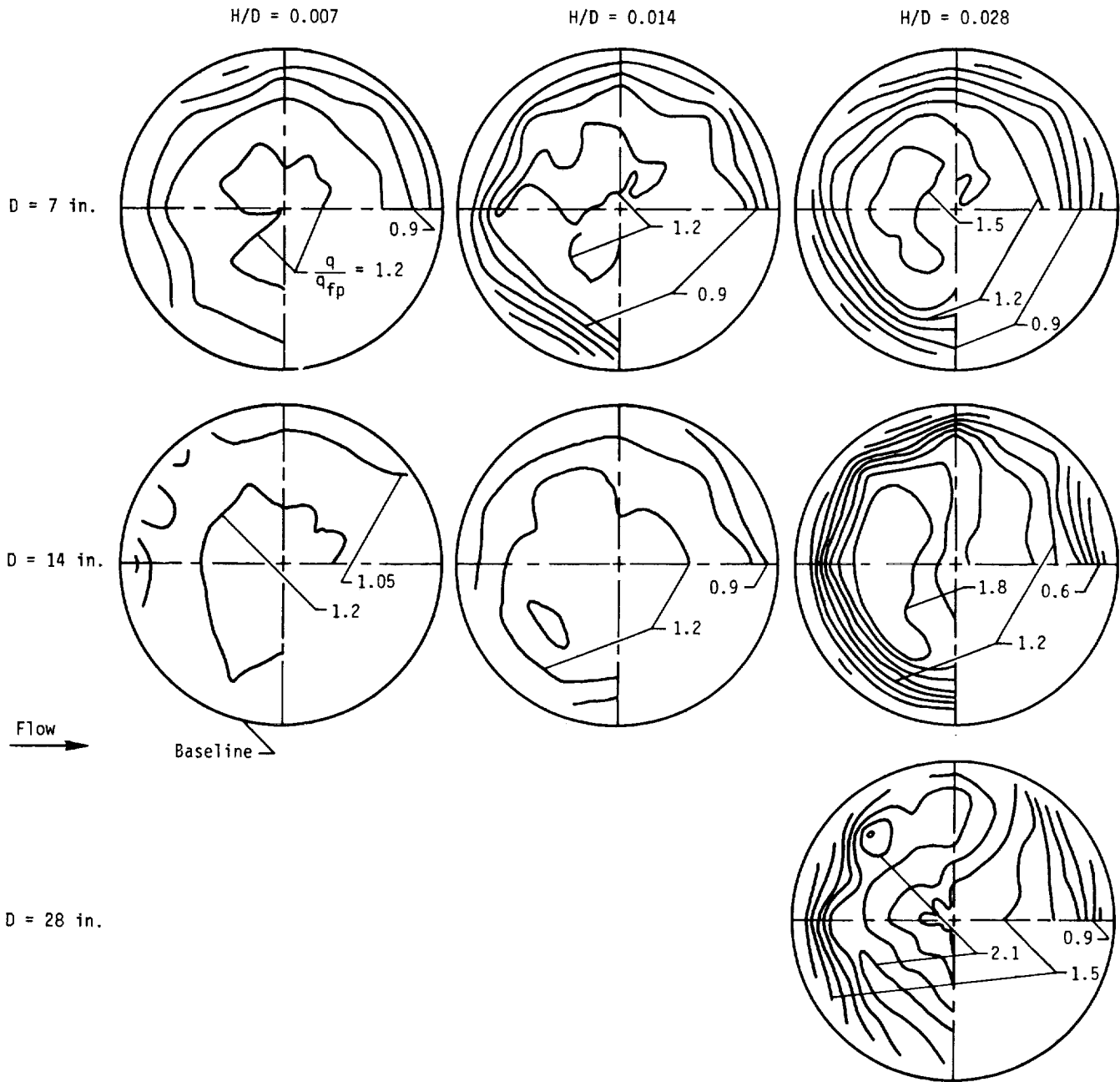
(a) Laminar boundary layer with blunt leading edge (no trips). Case 1.

Figure 17. Overview of normalized heating-rate contour. Nominal H/D conditions.

H/D = 0.007   H/D = 0.014   H/D = 0.028

D = 7 in.

$$\frac{q}{q_{fp}} = 1.2$$

0.9

0.9

1.05

1.2   0.6
0.9

D = 14 in.

1.05
1.2

0.9
1.2

1.2   0.9
1.5

Flow

Baseline

D = 28 in.

1.5   0.9
1.2
1.5
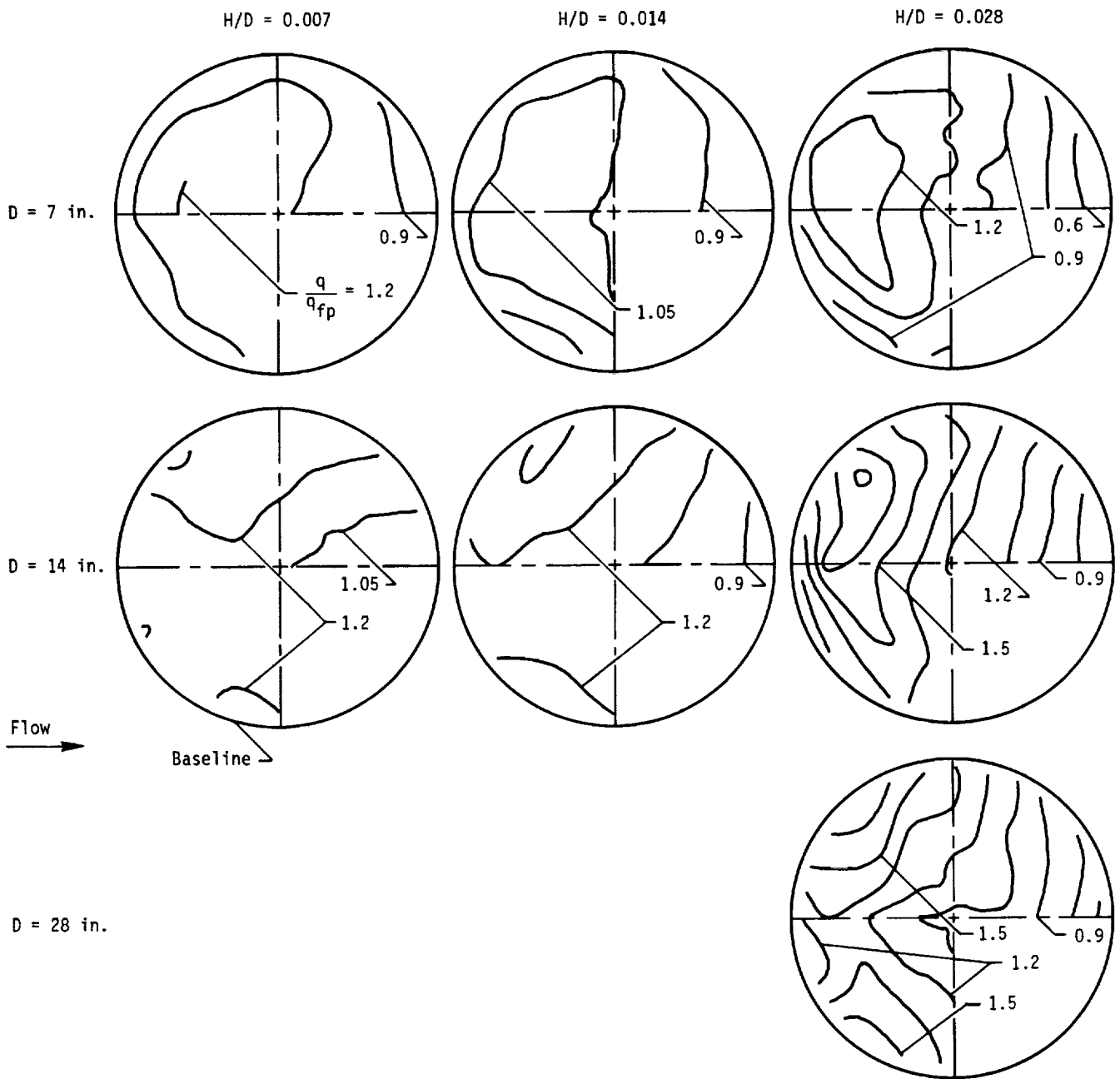
(b) Turbulent boundary layer with blunt leading edge (with trips). Case 2.

Figure 17. Continued.

48
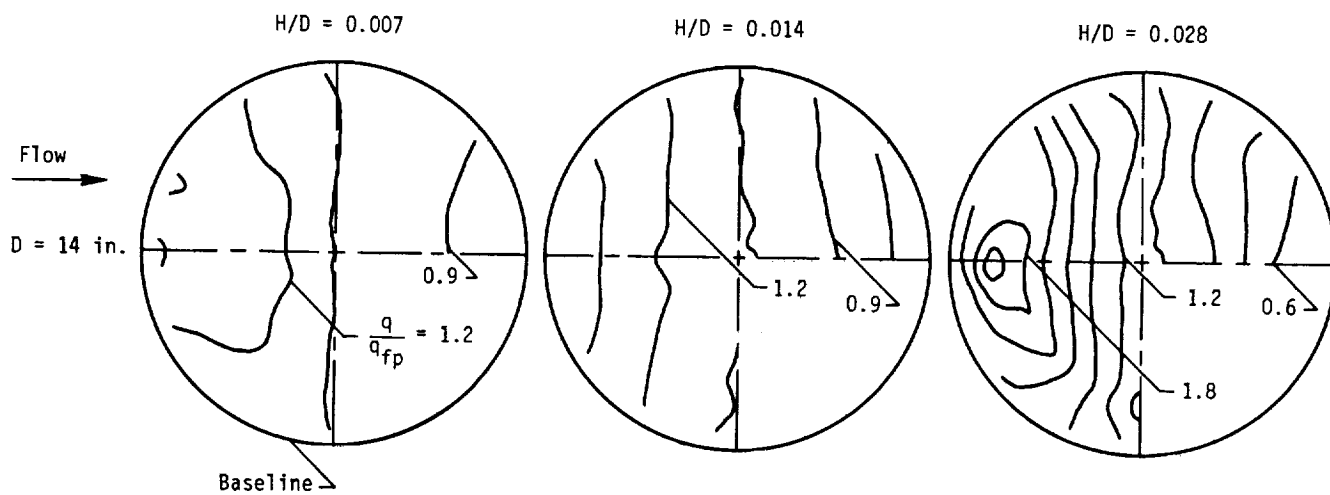
(c) Turbulent boundary layer with sharp leading edge (with trips). Case 3.

Figure 17. Concluded.
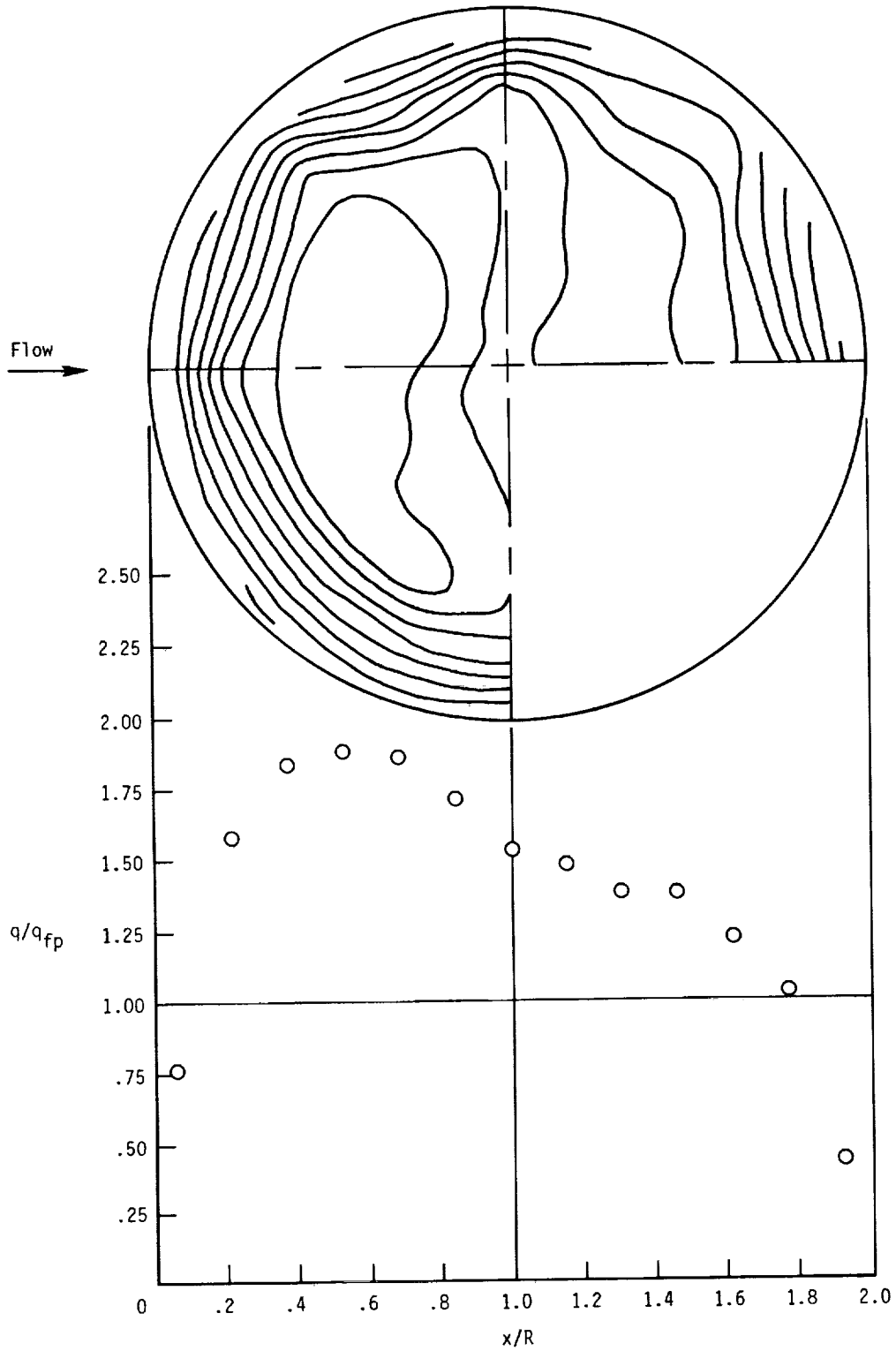
(a) Laminar boundary layer with blunt leading edge (no trips). Case 1.

Figure 18. Contour and longitudinal heating-rate distributions. $D = 14$ in.; $H = 0.4$ in.
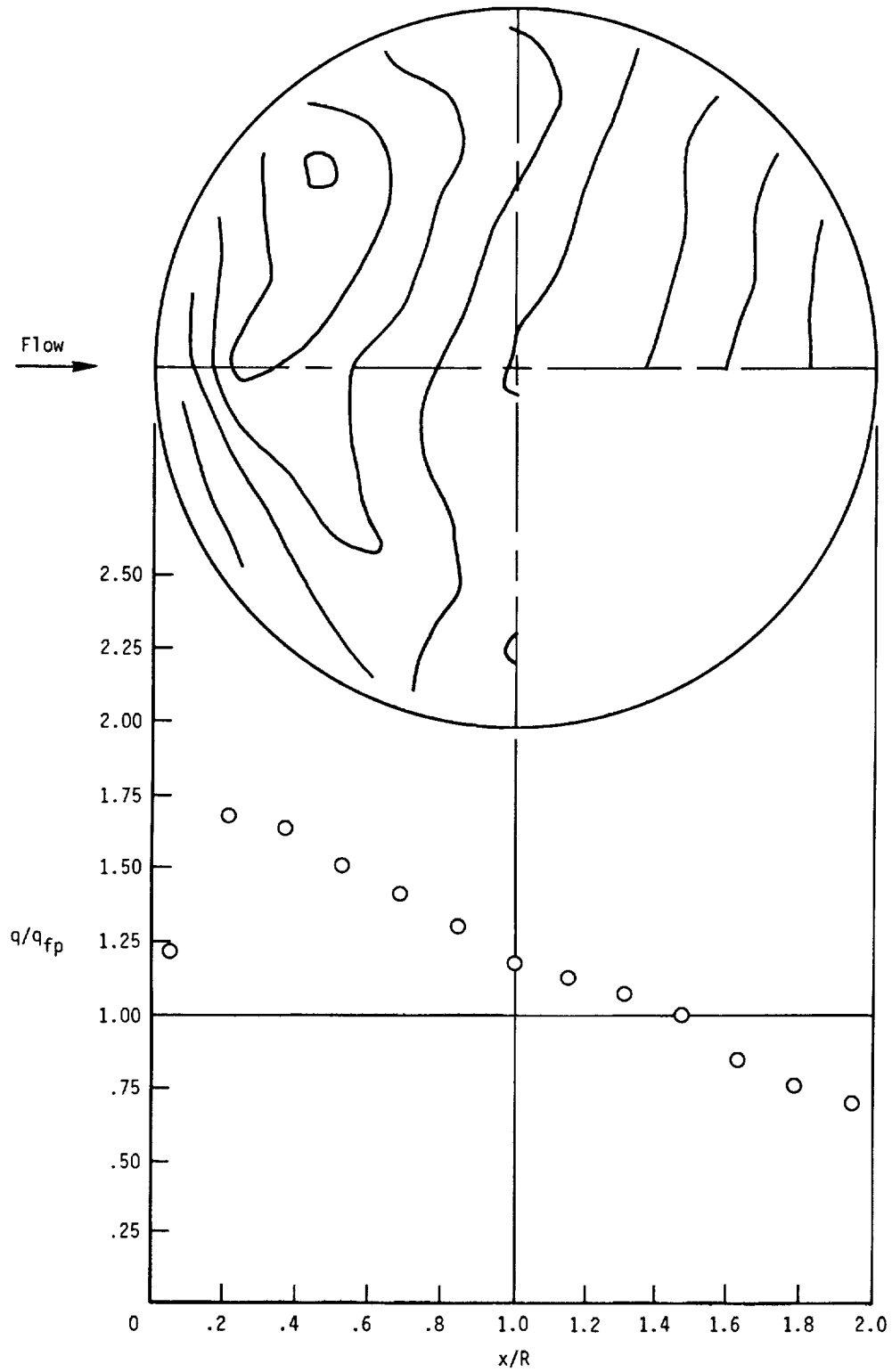
(b) Turbulent boundary layer with blunt leading edge (with trips). Case 2.

Figure 18. Continued.
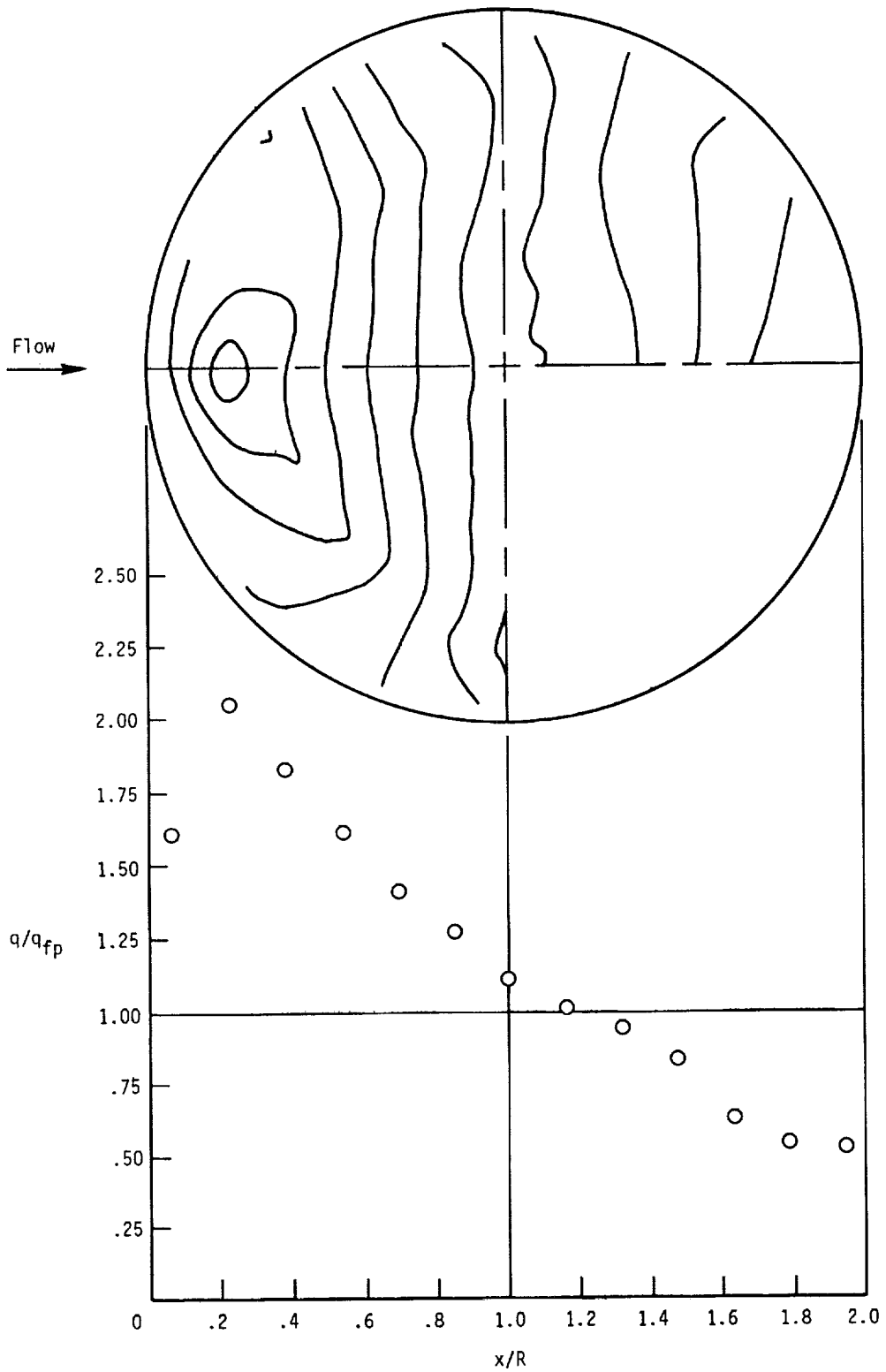
(c) Turbulent boundary layer with sharp leading edge (with trips). Case 3.

Figure 18. Concluded.
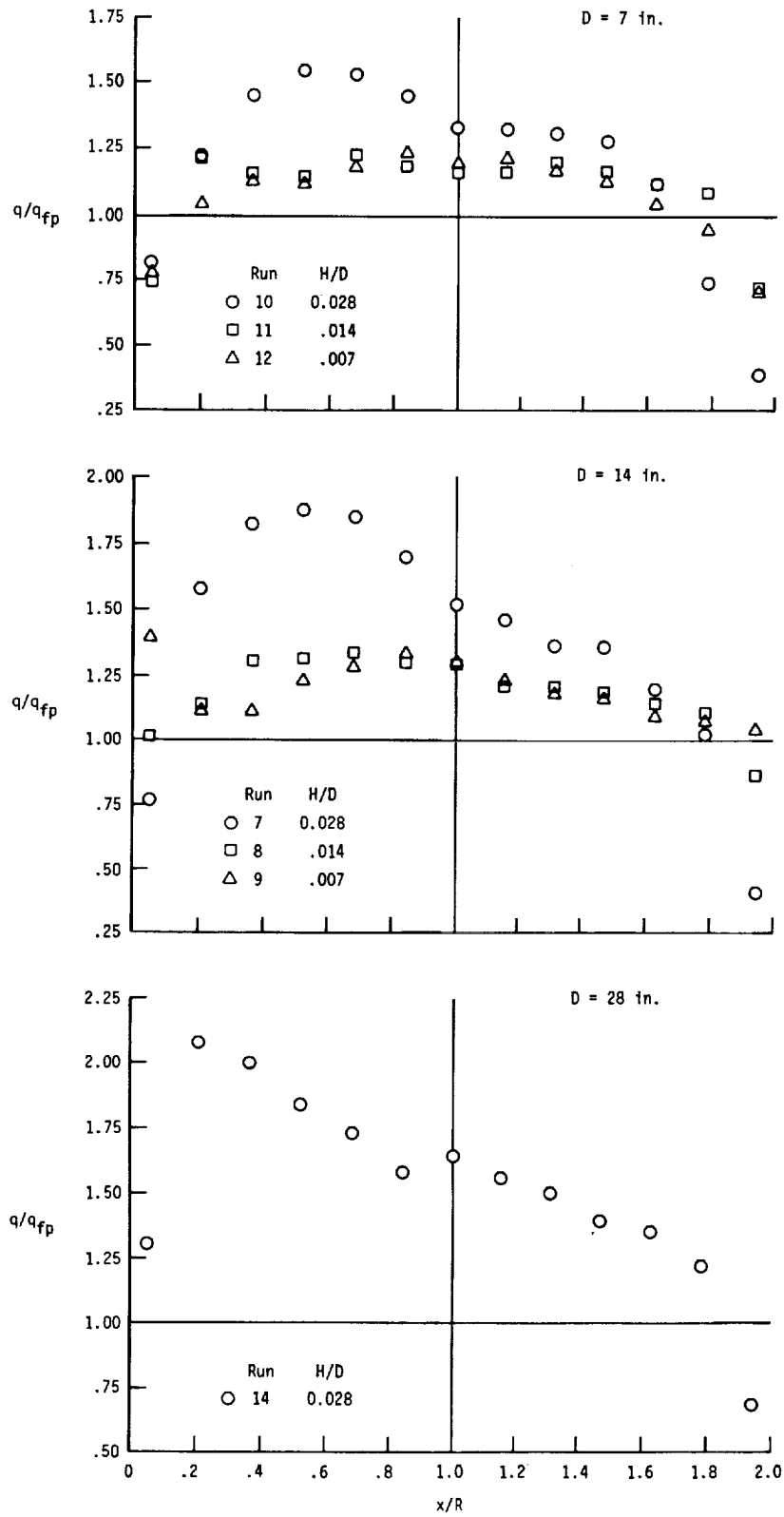
(a) Laminar boundary layer with blunt leading edge (no trips). Case 1; run 9 is baseline condition.

Figure 19. Longitudinal heating-rate distributions on protuberances.
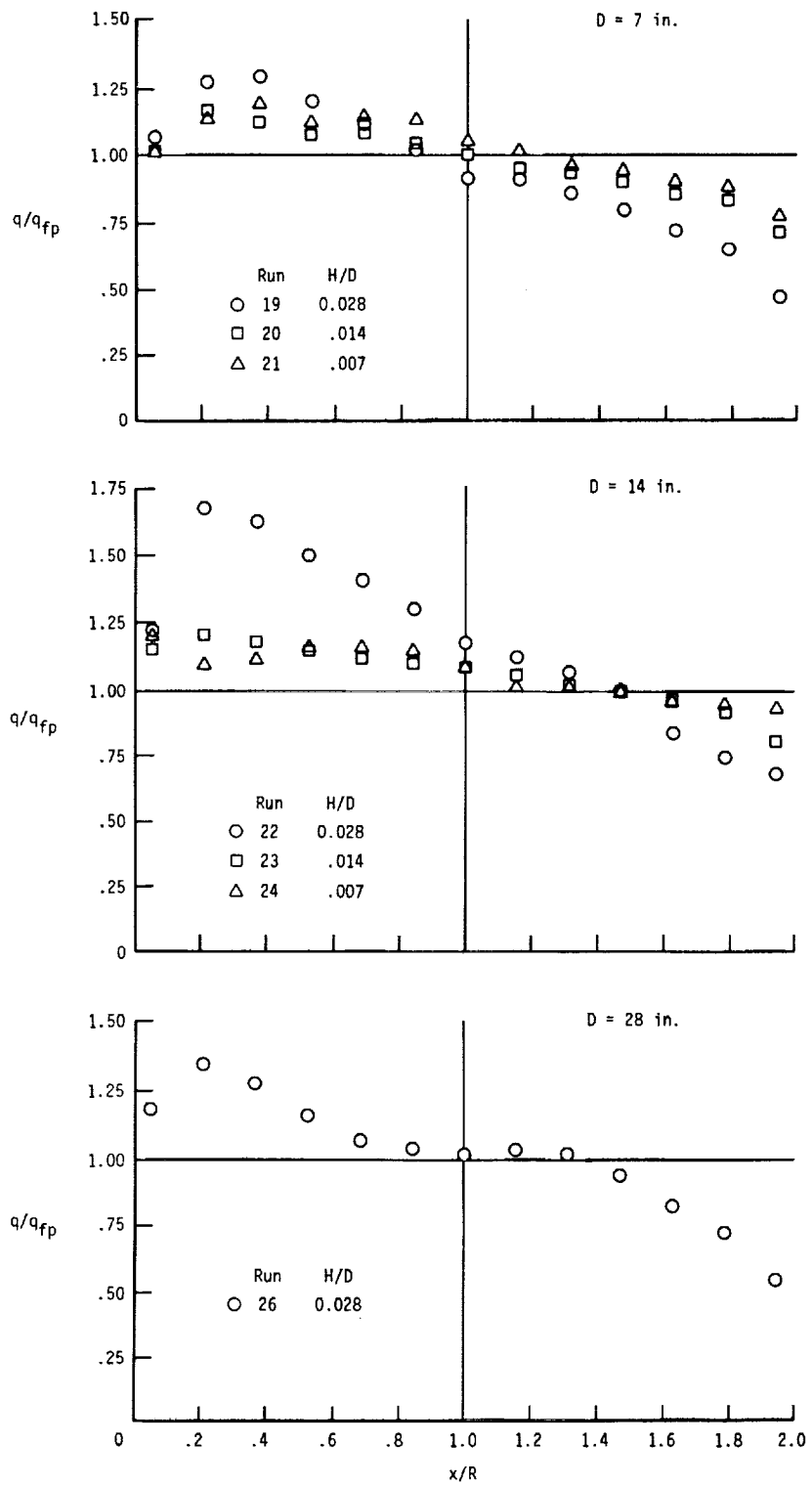
(b) Turbulent boundary layer with blunt leading edge (with trips). Case 2; run 24 is baseline condition.

Figure 19. Continued.
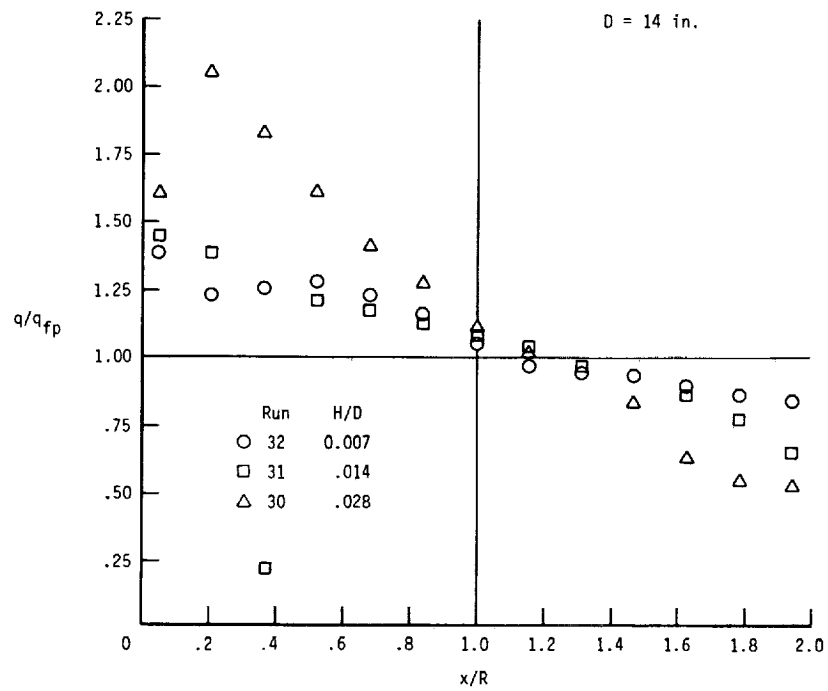
(c) Turbulent boundary layer with sharp leading edge (with trips). Case 3; run 32 is baseline condition.

Figure 19. Concluded.
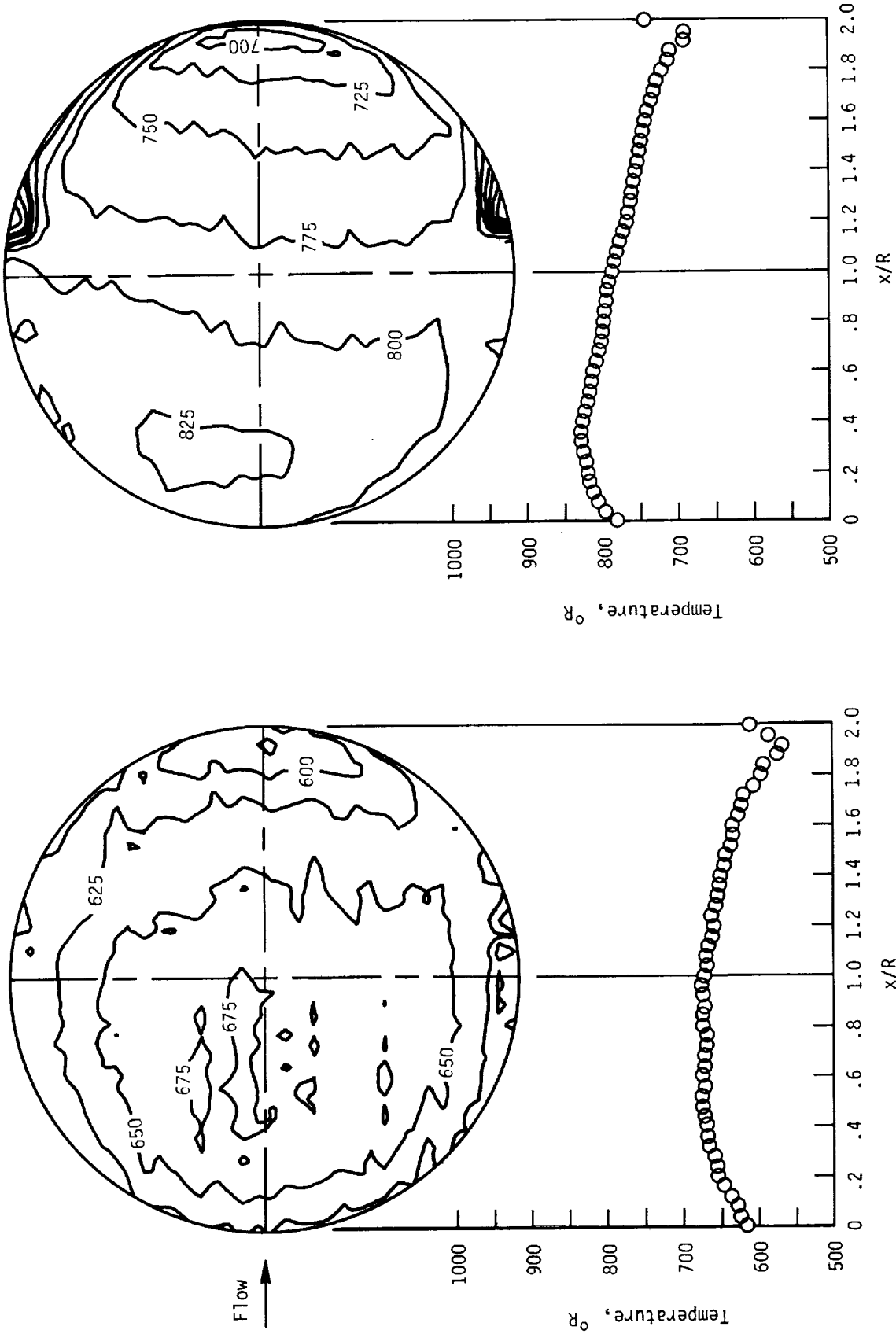
(a) Laminar boundary layer with blunt
leading edge (no trips). Case 1.

(b) Turbulent boundary layer with blunt
leading edge (with trips). Case 2.

Figure 20. Temperature distributions of ceramic dome. $D = 7$ in.; $H = 0.2$ in.
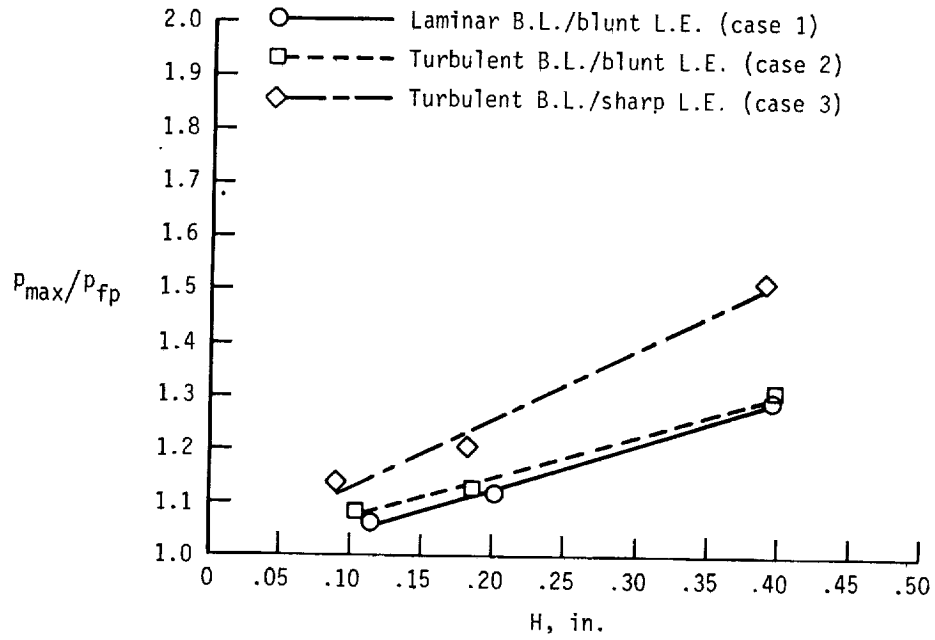
Figure 21. Peak pressure along longitudinal centerline. $D = 14$ in.
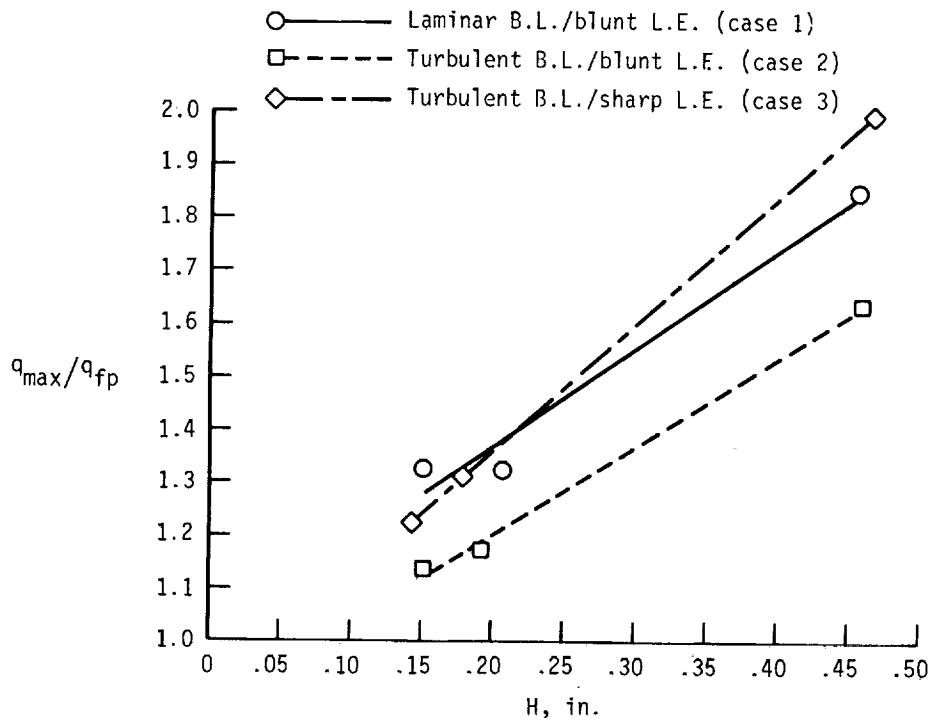
Figure 22. Peak heating rate along longitudinal centerline. $D = 14$ in.
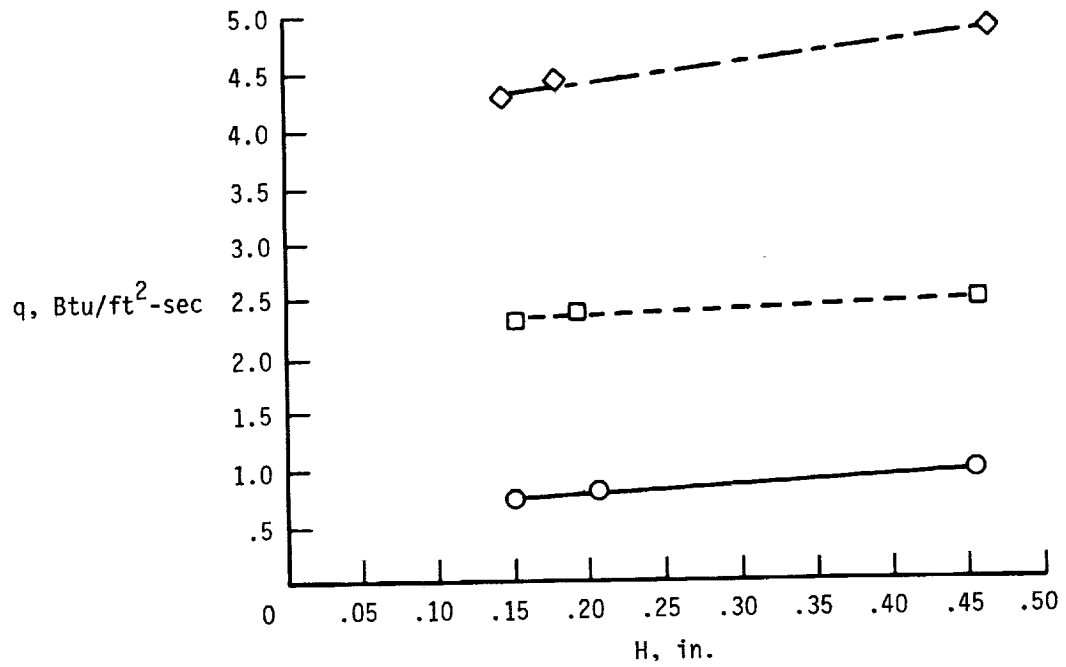
(a) Absolute heat load per unit area.
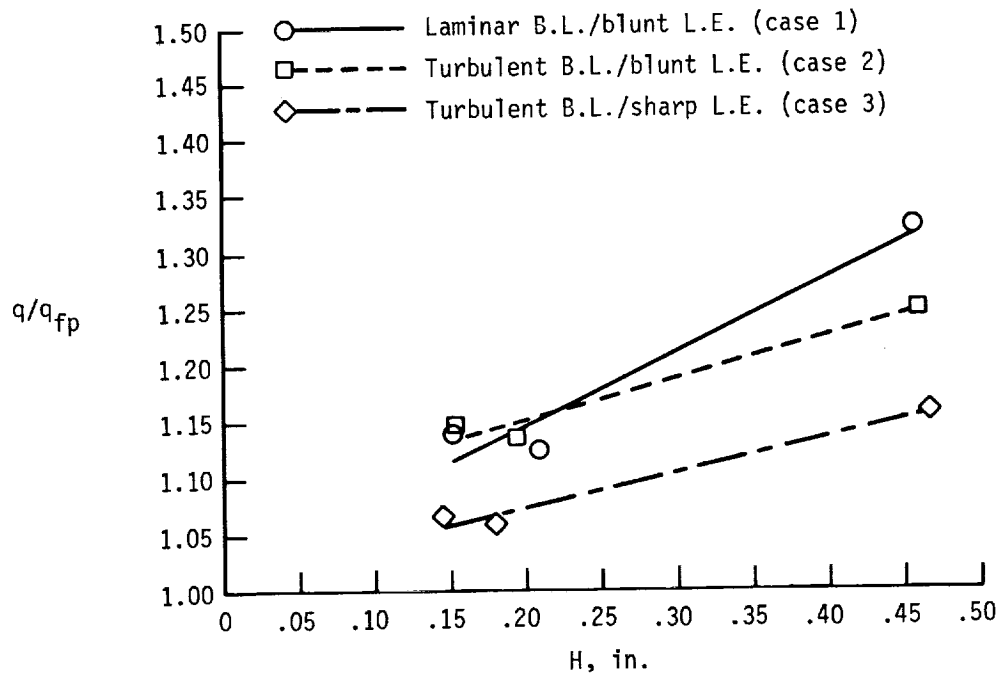
(b) Normalized heat load.

Figure 23. Total integrated heat load on protuberance. $D = 14$ in.

Standard Bibliographic Page

1. Report No. NASA TP-2631	2. Government Accession No.	3. Recipient's Catalog No.
4. Title and Subtitle Aerothermal Tests of Spherical Dome Protuberances on a Flat Plate at a Mach Number of 6.5		5. Report Date December 1986
		6. Performing Organization Code 506-40-21-01
7. Author(s) Christopher E. Glass and L. Roane Hunt		8. Performing Organization Report No. L-16160
9. Performing Organization Name and Address NASA Langley Research Center Hampton, VA 23665-5225		10. Work Unit No.
		11. Contract or Grant No.
12. Sponsoring Agency Name and Address National Aeronautics and Space Administration Washington, DC 20546-0001		13. Type of Report and Period Covered Technical Paper
		14. Sponsoring Agency Code

15. Supplementary Notes

16. Abstract

Aerothermal tests were conducted in the Langley 8-Foot High-Temperature Tunnel at a Mach number of 6.5 on a series of spherical dome protuberances mounted on a flat-plate test apparatus. Detailed surface pressure and heating-rate distributions were obtained for various dome heights and diameters submerged in both laminar and turbulent boundary layers including a baseline geometric condition representing a thermally bowed metallic thermal protection system (TPS) tile. The present results indicated that the surface pressures on the domes were increased on the windward surface and reduced on the leeward surface as predicted by linearized small-perturbation theory, and the distributions were only moderately affected by boundary-layer variations. Surface heating rates for turbulent flow increased on the windward surface and decreased on the leeward surface similar to the pressure; but for laminar boundary layers, the heating rates remained high on the leeward surface, probably due to local transition. Transitional flow effects caused heat load augmentation to increase by 30 percent for the maximum dome height in a laminar boundary layer. However, the corresponding augmentation for a dome with a height of 0.1 in. and a diameter of 14 in. representative of a bowed TPS tile was 14 percent or less for either a laminar or turbulent boundary layer.

| 17. Key Words (Suggested by Authors(s))
Hypersonic flight vehicle
Thermal protection system
Protuberance
Pressure and heating-rate distributions
Laminar and turbulent boundary layers | 18. Distribution Statement
Unclassified—Unlimited

Subject Category 34 | | |
| 19. Security Classif.(of this report)
Unclassified | 20. Security Classif.(of this page)
Unclassified | 21. No. of Pages
59 | 22. Price
A04 |